Fast Scalar Quadratic Maximum Likelihood Estimators for the CMB *B*-mode Power Spectrum

Jiming Chen[1,2] , Shamik Ghosh[1,2] , Hao Liu[3] , Larissa Santos[4,5], Wenjuan Fang[1,2], Siyu Li[6], Yang Liu[6], Hong Li[6],
Jiaxin Wang[7], Le Zhang[8] , Bin Hu[9] , and Wen Zhao[1,2]

[1] CAS Key Laboratory for Researches in Galaxies and Cosmology, Department of Astronomy, University of Science and Technology of China, Chinese Academy of
Sciences, Hefei, Anhui 230026, People's Republic of China; chenjm94@mail.ustc.edu.cn, shamik@ustc.edu.cn, wzhao7@ustc.edu.cn
[2] School of Astronomy and Space Science, University of Science and Technology of China, Hefei 230026, People's Republic of China
[3] School of Physics and Material Science, Anhui University, 111 Jiulong Road, Hefei, Anhui 230601, People's Republic of China
[4] Center for Gravitation and Cosmology, College of Physical Science and Technology, Yangzhou University, Yangzhou 225009, People's Republic of China
[5] School of Aeronautics and Astronautics, Shanghai Jiao Tong University, Shanghai, 200240, People's Republic of China
[6] Institute of High Energy Physics, Chinese Academy of Sciences, Beijing 100049, People's Republic of China
[7] Department of Astronomy, Shanghai Jiao Tong University, Shanghai 200240, People's Republic of China
[8] School of Physics and Astronomy, Sun Yat-Sen University, 2 Daxue Road, Tangjia, Zhuhai 519082, People's Republic of China
[9] Department of Astronomy, Beijing Normal University, Beijing 100875, People's Republic of China

Abstract

Constructing a fast and efficient estimator for the *B*-mode power spectrum of the cosmic microwave background (CMB) is of critical importance for CMB science. For a general CMB survey, the Quadratic Maximum Likelihood (QML) estimator for CMB polarization has been proved to be the optimal estimator with minimal uncertainties, but it is computationally very expensive. In this article, we propose two new QML methods for *B*-mode power spectrum estimation. We use the Smith–Zaldarriaga approach to prepare the pure *B*-mode map and the *E*-mode recycling method to obtain a leakage free *B*-mode map. We then use the scalar QML estimator to analyze the scalar pure *B* map (QML-SZ) or *B*-mode map (QML-TC). The QML-SZ and QML-TC estimators have similar error bars as the standard QML estimators but their computational cost is nearly one order of magnitude smaller. The basic idea is that one can construct the pure *B*-mode CMB map by using the *E*–*B* separation method proposed by Smith & Zaldarriaga (SZ) or the one considering the template cleaning (TC) technique, then apply the QML estimator to these scalar fields. By simulating potential observations of space-based and ground-based detectors, we test the reliability of these estimators by comparing them with the corresponding results of the traditional QML estimator and the pure *B*-mode pseudo-C_ℓ estimator.

1. Introduction

The reliable characterization and scientific exploitation of the polarized cosmic microwave background (CMB) signal will provide a wealth of information about the dynamical evolution of the universe (Kamionkowski et al. 1997; Seljak & Zaldarriaga 1997; Zhao et al. 2009, 2010; Zhao & Grishchuk 2010) and the nature of both dark matter (Górski et al. 2005; Bucher et al. 2001) and dark energy (Giovi et al. 2003). Polarized anisotropies of the CMB radiation can be separated into *E*-mode and the *B*-mode components (Zaldarriaga & Seljak 1997; Kamionkowski et al. 1997; Pritchard & Kamionkowski 2005; Zhao & Zhang 2006; Baskaran et al. 2006; Flauger & Weinberg 2007). In the past two decades, many experiments, e.g., DASI (Kovac et al. 2002), the Wilkinson Microwave Anisotropy Probe (Benabed et al. 2001; Hinshaw et al. 2007; Komatsu et al. 2011), BOOMERanG (Montroy et al. 2006), QUAD (Brown et al. 2009), BICEP (Chiang et al. 2010), QUIET (QUIET Collaboration et al. 2012), ACT (Naess et al. 2014), Planck (Planck Collaboration et al. 2014), and SPTpol (Henning et al. 2018) have already detected the *E*-mode signal with a high confidence level. For instance, the Planck satellite experiment provides precise constraints on the *E*-mode polarization properties in a wide range of angular scales.

The detection of the large-scale *B*-mode polarization would indicate the presence of a stochastic background of gravitational waves, which may be a leftover from the inflationary epoch in the early universe (Grishchuk 1974; Hu et al. 1997; Linde et al. 1999; Liddle & Lyth 2000; Kamionkowski et al. 1997; Seljak & Zaldarriaga 1997; Ma et al. 2010). However, the *B*-mode signal is dominated by lensed *B* modes produced by the weak gravitational lensing effect of the CMB photons during their travel from the last scattering surface to us (Zaldarriaga & Seljak 1998), which converts the *E* modes into *B* modes. Great effort has been made to observe the CMB *B* modes with ongoing ground-based experiments, such as BICEP-3 (Ahmed et al. 2014), AdvACTPol (Henderson et al. 2016), and SPT-3G (Benson et al. 2014). Other upcoming experiments, like AliCPT-1 (Li et al. 2017; Salatino et al. 2021), Simons Observatory (Ade et al. 2019), LSPE (The LSPE Collaboration et al. 2012), QUIJOTE (Pérez-de-Taoro et al. 2014), and CMB-S4 (The CMB-S4 Collaboration et al. 2020), will join the efforts to look for the primordial CMB *B* modes from the ground, while the future LiteBIRD (Hazumi et al. 2019) satellite aims to observe the CMB polarized signal from space.

The CMB *B*-mode signal is much fainter than the *E*-mode. Its detection is then greatly limited by polarized astrophysical foregrounds, primarily dominated by dust and synchrotron emissions. Even if we are able to obtain clean maps by perfectly removing these foregrounds, we still face the challenge of dealing with the *E*–*B* leakage, which arises from *E*–*B* decomposition on an incomplete sky (Tegmark & de Oliveira-Costa 2001). In the partial sky case, the polarization

Satellite experiment
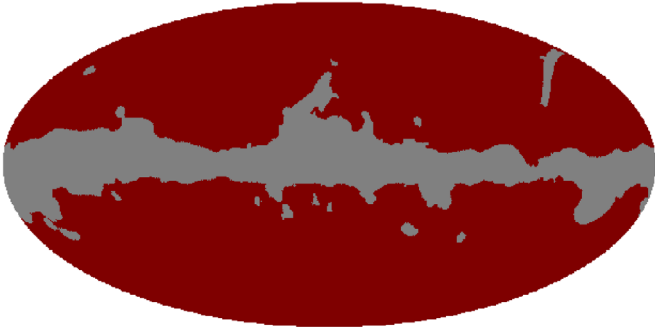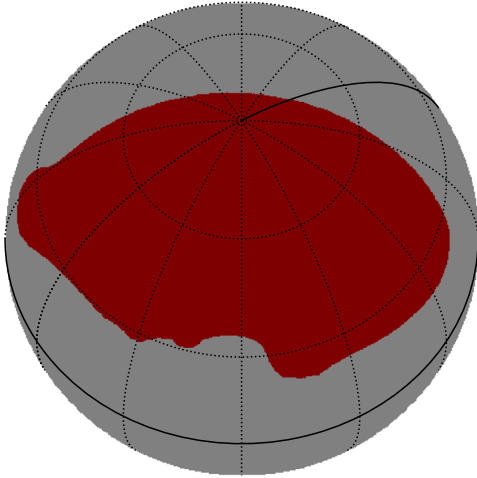
Small-scale experiment

Figure 1. Binary masks showing the observed sky patch for a space-based experiment (top) and for a ground-based experiment (bottom) as considered in this work. The red area is the observed area and the gray area is the mask area. The plots are in the Galactic coordinate system. The sky fractions are 78.8% and 15.1%, respectively.

field cannot be uniquely decomposed into E and B modes due to the ambiguity in the relationship between the Stokes parameters, and therefore in the E and B modes (Bunn et al. 2003; Bunn 2008). In short, besides the ambiguous modes, the complete B-mode information consists of both the primordial and the lensed signal. Even though no bias is directly introduced, this leakage will play an important role in isolating the cosmological B-mode power spectrum from the input partial sky maps due to the increase of the overall uncertainty of the estimated signal.

Various methods have been proposed to alleviate the E–B mixing problem and restore the cosmological B-mode information from an incomplete sky coverage, including several extensions of the standard pseudo-C_ℓ (PCL) methods (Hivon et al. 2002; Hansen & Górski 2003; Smith 2006; Smith & Zaldarriaga 2007; Zhao & Baskaran 2010; Kim & Naselsky 2010; Kim 2011; Grain et al. 2012; Liu et al. 2019a; Ghosh et al. 2021), which solve for the power spectra by inverting the linear system relating the full sky power to the power from incomplete sky. These methods use fast spherical harmonic transforms with the advantage of speeding up their computation. The method proposed in Smith (2006) and

Smith & Zaldarriaga (2007), hereafter the SZ method, was shown to be the PCL estimator (Ferté et al. 2013) with the smallest errors. In our paper, we consider the SZ method using an analytically apodized window function.

The Gibbs sampling technique (Jewell et al. 2004; Wandelt et al. 2004; Larson et al. 2007) may provide a unified way to jointly estimate pure E- and B-mode spectra and maps from a masked polarization sky, since this technique circumvents the E/B decomposition by sampling full sky realizations of the polarization in terms of their likelihood. However, the Gibbs sampling technique suffers a convergence issue in the low-signal-to-noise ratio regime and would take a long convergence time for B-mode spectra to be estimated correctly. Generalized Wiener filtering methods can also been used for E/B decomposition (Bunn & Wandelt 2017; Kodi Ramanah et al. 2018, 2019).

The Quadratic Maximum Likelihood (QML) method (Tegmark & de Oliveira-Costa 2001), which is a pixel-based estimator, provides another way to solve the E–B mixing problem. It has the advantage of minimizing spectra uncertainties, but, at the same time, it involves matrix inversions and multiplications that significantly increase the calculation time and the demand for computational memory.

Recently, another method was proposed to partly solve the E–B mixture problem (Liu et al. 2019a). Based on the available high-precision E-mode data sets, the template cleaning (TC) method can be used to estimate the E–B leakage that will be later removed from the observed CMB maps. Finally, we can use an appropriate method to reconstruct the B-mode power spectrum from "real" B maps.

Combining the advantages of the above three methods, we propose two new methods to reconstruct the large-scale B-mode power spectrum: the QML-SZ method and the QML-TC method. The QML-SZ method uses the SZ method to derive the pure B-mode map $\mathcal{B}(\hat{n})$ from Stokes Q and U maps, which can be ultimately treated as scalar fields, enabling us to use the QML method developed for CMB temperature maps. Similarly, in the QML-TC method, we can first use the template cleaning method to get the leakage free B-mode map from Q and U maps, and then use the scalar-mode QML method to estimate the B-mode power spectrum. Since we adopt the SZ and/or template cleaning methods to transform the Stokes Q and U maps into scalar B-mode maps, the number of pixels drops to $1/2$ that of the standard QML method. This means that the computational running time will be eight times shorter than for the standard QML estimator. We are able to precisely reconstruct an unbiased power spectrum with reasonably small errors using the methodology described above, with the advantage of drastically reducing our computational requirements.

This paper organized as follows. In Section 2, we review the traditional QML method first. Next, we introduce the SZ method and combine it with scalar QML method to construct the QML-SZ estimator. After that, we briefly introduce the template cleaning method and adopt the scalar QML method to construct the QML-TC estimator. In Section 3, we test the effects of various factors that may affect the uncertainties of these two estimators. In Section 4, we apply the these methods to more realistic situations and make a comprehensive comparison of their performance. Conclusions and discussions are given in Section 5.
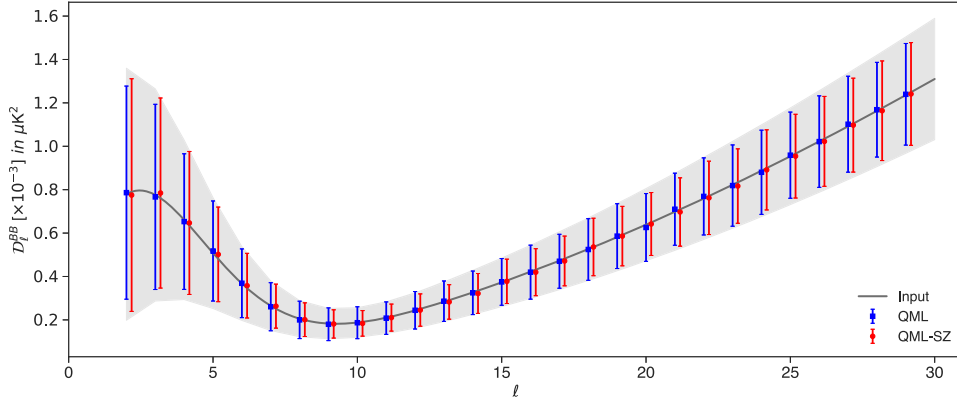
Figure 2. Plot of *B*-mode power spectrum estimates for testing the effects of f_{sky} for the space-based experiment. The input *B*-mode power spectrum is represented by the black curve, the blue square markers indicate the classic QML method estimators, and the red circle markers show results from the QML-SZ scalar method. The gray band shows the error bars calculated with the analytical formula in Equation (50).
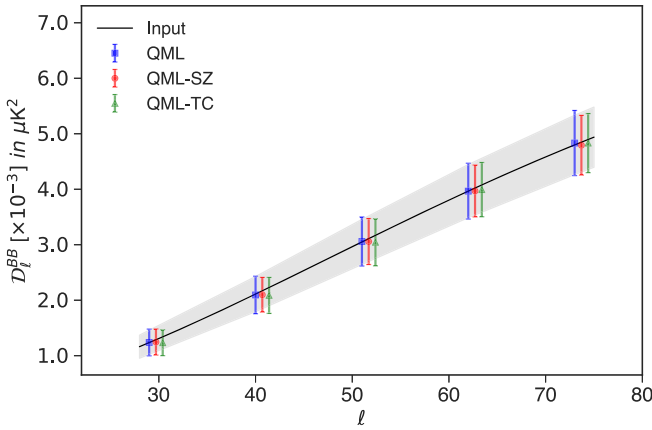

Figure 3. Plot of *B*-mode power spectrum estimates for testing the effects of f_{sky} for the ground-based experiment. The input *B*-mode power spectrum is represented by the black curve, the blue square markers indicate the classic QML method estimators, the red circle markers show results from the QML-SZ scalar method, and the green triangle markers show the QML-TC estimators. The gray band shows the error bars calculated with the analytical formula in Equation (50).

2. Power Spectrum Estimators

2.1. E–B Mixture in Partial Sky Surveys

The linear polarization of the CMB field can be completely described by the Stokes parameters Q and U. Along the line of sight, $\hat{n}$, the polarization field can be written as:

$$P_\pm(\hat{n}) = Q(\hat{n}) \pm iU(\hat{n}), \qquad (1)$$

which behaves as a spin-(2) and a spin-(−2) field. In the simplest full sky case, these fields are expanded over spin-weighted spherical harmonics, $_{\pm s}Y_{\ell m}$, as (Seljak & Zaldarriaga 1996):

$$P_\pm(\hat{n}) = \sum_{\ell m} a_{\pm 2, \ell m} \, _{\pm 2}Y_{\ell m}(\hat{n}). \qquad (2)$$

Detailed expressions are given in Appendix A.

However, describing the polarization field by means of the the Stokes parameters is frame dependent. Therefore, for convenience, we write the polarization field in terms of the rotationally invariant E and B components. These components are defined in the harmonic space in terms of spin-harmonic coefficients $a_{\pm 2, \ell m}$.

$$a_{E,\ell m} \equiv -\frac{1}{2}[a_{2,\ell m} + a_{-2,\ell m}]$$
$$= -\frac{1}{2}\left[\int P_+(\hat{n})\,_2Y_{\ell m}^*(\hat{n})d\hat{n} + \int P_-(\hat{n})\,_{-2}Y_{\ell m}^*(\hat{n})d\hat{n}\right], \qquad (3)$$

$$a_{B,\ell m} \equiv -\frac{1}{2i}[a_{2,\ell m} - a_{-2,\ell m}]$$
$$= \frac{i}{2}\left[\int P_+(\hat{n})\,_2Y_{\ell m}^*(\hat{n})d\hat{n} - \int P_-(\hat{n})\,_{-2}Y_{\ell m}^*(\hat{n})d\hat{n}\right]. \qquad (4)$$

We can then define the $E(\hat{n})$ and $B(\hat{n})$ sky maps as:

$$E(\hat{n}) \equiv \sum_{\ell m} a_{E,\ell m} Y_{\ell m}(\hat{n}), \qquad B(\hat{n}) \equiv \sum_{\ell m} a_{B,\ell m} Y_{\ell m}(\hat{n}). \qquad (5)$$

Finally, the power spectra can be obtained as follows

$$C_\ell^{EE} \equiv \langle E_{\ell m} E_{\ell m}^* \rangle, \qquad C_\ell^{BB} \equiv \langle B_{\ell m} B_{\ell m}^* \rangle, \qquad (6)$$

where the angular brackets denote the average over realizations.

For an incomplete sky observation, defined by the window function $W(\hat{n})$, in principle, we can also define the partial sky E- and B-mode spherical harmonic coefficients (indicated by the overhead tilde) as:

$$\tilde{a}_{E,\ell m} = -\frac{1}{2}\left[\int P_+ \, W \, _2Y_{\ell m}^* d\hat{n} + \int P_- \, W \, _{-2}Y_{\ell m}^* d\hat{n}\right], \qquad (7)$$

$$\tilde{a}_{B,\ell m} = \frac{i}{2}\left[\int P_+ \, W \, _2Y_{\ell m}^* d\hat{n} - \int P_- \, W \, _{-2}Y_{\ell m}^* d\hat{n}\right]. \qquad (8)$$

These coefficients $\tilde{a}_{E,\ell m}$ and $\tilde{a}_{B,\ell m}$ relate to the pure E and B coefficients $a_{E,\ell m}$ and $a_{B,\ell m}$ as follows:

$$\tilde{a}_{E,\ell m} = \sum_{\ell' m'}[K^{EE}_{\ell m \ell' m'} a_{E,\ell' m'} + iK^{EB}_{\ell m \ell' m'} a_{B,\ell' m'}],$$
$$\tilde{a}_{B,\ell m} = \sum_{\ell' m'}[-iK^{BE}_{\ell m \ell' m'} a_{E,\ell' m'} + K^{BB}_{\ell m \ell' m'} a_{B,\ell' m'}]. \qquad (9)$$

The coupling matrices $K^{XY}_{\ell m \ell' m'}$ are the mixing kernels for the partial sky observation, and the full form of these matrices can be found in Grain et al. (2009). Various methods have already been proposed to avoid the mixing by constructing the pure *E*-type and pure *B*-type fields, such as Bunn et al. (2003), Bunn (2011), Lewis (2003), Cao & Fang (2009), Louis et al. (2013), Grain et al. (2009), Smith (2006), Smith & Zaldarriaga (2007),
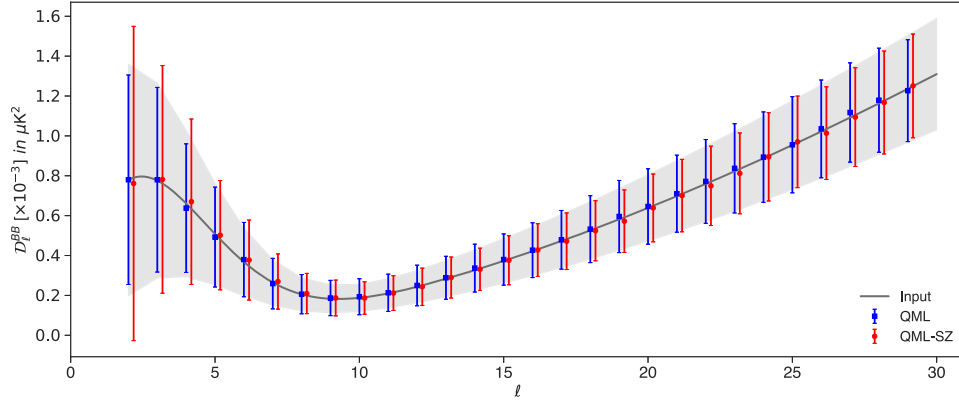
Figure 4. Plot of power spectrum estimates for testing the impacts of `ud_grade` for the space-based experiment. All maps are produced at `NSIDE = 512` with $\ell_{max} = 32$, and then downgraded to `NSIDE = 16`. The input *B*-mode power spectrum is represented by the black curve, the blue square markers indicate the classic QML method estimates, and the red circle markers show results from the QML-SZ scalar method. The gray band shows the optimal error limit from cosmic variance and noise variance.
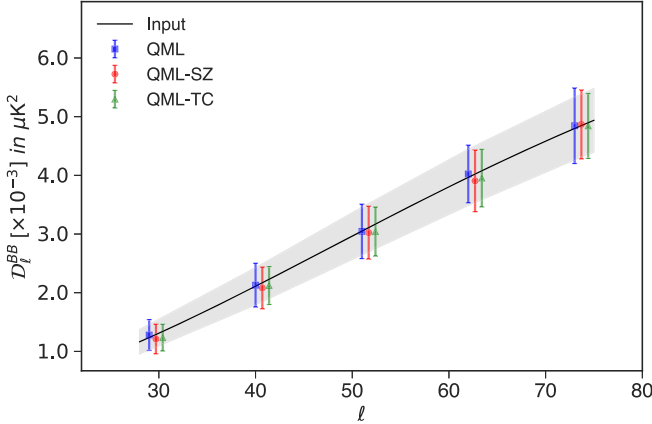

Figure 5. Plot of power spectrum estimates for testing the impacts of `ud_grade` for the ground-based experiment. All maps are produced at `NSIDE = 512` with $\ell_{max} = 96$, and then downgraded to `NSIDE = 32`. The input *B*-mode power spectrum is represented by the black curve, the blue square markers indicate the classic QML method estimates, the red circle markers show results from the QML-SZ scalar method, and the green triangle markers show the QML-TC estimates. The gray band shows the optimal error limit from cosmic variance and noise variance.

Zhao & Baskaran (2010), Kim & Naselsky (2010), Santos et al. (2016), and Santos et al. (2017).

2.2. Standard QML Estimator

In this article, we mainly focus on how to construct the fast estimators of the CMB *B*-mode power spectrum with small errors. For CMB polarization maps with any sky coverage, Tegmark (1997) defines a QML estimator for the CMB temperature power spectrum, which is generalized for CMB polarization power spectra by Tegmark & de Oliveira-Costa (2001). In this section, we briefly review the QML estimator for polarization. In the pixel domain, we can define an input data vector, x, which consists of the temperature fluctuation field and the Stokes Q and U (with respect to a fixed coordinate system) specified at the ith pixel as

$$x_i = \begin{pmatrix} \Delta T_i \\ Q_i \\ U_i \end{pmatrix} + \begin{pmatrix} n_i^T \\ n_i^Q \\ n_i^U \end{pmatrix}. \qquad (10)$$

Following Tegmark & de Oliveira-Costa (2001), the optimal quadratic estimate of the power spectrum, y_ℓ^r, is defined as :

$$y_\ell^r = x_i^t E_{ij}^{r\ell} x_j - b_\ell^r, \qquad r \in [T, TE, E, B], \qquad (11)$$

where t indicates a matrix transpose operation. Here, r is the index denoting the power spectrum and i, j are indices over pixels. The data x_i at a particular pixel are a *TQU* component vector and $E_{ij}^{r\ell}$ is a 3×3 matrix. The bias vector, b_ℓ^r, corrects for the noise bias and is given by $\mathrm{Tr}[E_\ell^r N]$, when the noise, n, is uncorrelated between pixels. Note that we have assumed the summation convention. The $E^{r\ell}$ matrices are computed as:

$$E^{r\ell} = \frac{1}{2} C^{-1} \frac{\partial C}{\partial C_\ell^r} C^{-1} \qquad (12)$$

and the covariance matrix of the data x, denoted by C, is:

$$
\begin{aligned}
C_{ij} = \langle x_i x_j^t \rangle &= R(\alpha_{ij}) M(\hat{r}_i \cdot \hat{r}_j) R(\alpha_{ji})^t + N_{ij} \\
&= \begin{pmatrix} C_{ij}^{TT} & C_{ij}^{TQ} & C_{ij}^{TU} \\ C_{ij}^{QT} & C_{ij}^{QQ} & C_{ij}^{QU} \\ C_{ij}^{UT} & C_{ij}^{UQ} & C_{ij}^{UU} \end{pmatrix},
\end{aligned} \qquad (13)
$$

where N is the noise covariance matrix and the rotation matrix R is given by:

$$R(\alpha_{ij}) = \begin{pmatrix} 1 & 0 & 0 \\ 0 & \cos(2\alpha_{ij}) & \sin(2\alpha_{ij}) \\ 0 & -\sin(2\alpha_{ij}) & \cos(2\alpha_{ij}) \end{pmatrix}, \qquad (14)$$

which performs a rotation to a global frame where the reference directions are given by the meridians. M is the covariance matrix when Q and U are defined with the reference direction being the great circle connecting the two points. So, it depends only on the angular separation between the two pixels. The explicit expression for this matrix is given by

$$M(\hat{r}_i \cdot \hat{r}_j) = \begin{pmatrix} \langle T_i T_j \rangle & \langle T_i Q_j \rangle & \langle T_i U_j \rangle \\ \langle Q_i T_j \rangle & \langle Q_i Q_j \rangle & \langle Q_i U_j \rangle \\ \langle U_i T_j \rangle & \langle U_i Q_j \rangle & \langle U_i U_j \rangle \end{pmatrix}, \qquad (15)$$

where

$$\langle T_i T_j \rangle = \sum_\ell \frac{2\ell + 1}{4\pi} C_\ell^{TT} P_\ell(z),$$

$$\langle T_i Q_j \rangle = -\sum_\ell \frac{2\ell + 1}{4\pi} C_\ell^{TE} F_\ell^{10}(z),$$

$$\langle T_i U_j \rangle = -\sum_\ell \frac{2\ell + 1}{4\pi} C_\ell^{TB} F_\ell^{10}(z),$$

$$\langle Q_i Q_j \rangle = \sum_\ell \frac{2\ell + 1}{4\pi} [C_\ell^{EE} F_\ell^{12}(z) - C_\ell^{BB} F_\ell^{22}(z)],$$

$$\langle U_i U_j \rangle = \sum_\ell \frac{2\ell + 1}{4\pi} [C_\ell^{BB} F_\ell^{12}(z) - C_\ell^{EE} F_\ell^{22}(z)],$$

$$\langle Q_i U_j \rangle = \sum_\ell \frac{2\ell + 1}{4\pi} [F_\ell^{12}(z) + F_\ell^{22}(z)] C_\ell^{EB}.$$

We have used $z = \hat{r}_i \cdot \hat{r}_j$ as the cosine of the angle between the ith and jth pixels. Note that P_ℓ denotes a Legendre polynomial, and the form of functions F_ℓ^{10}, F_ℓ^{12}, and F_ℓ^{22} are given in Appendix A.

Considering the matrix definitions given above, one can get minimum variance estimates of the CMB power spectra using Equation (11). From Equation (13), we find that the temperature fluctuation fields are coupled with the polarization fields. It has been pointed out by Tegmark & de Oliveira-Costa (2001) that this may be problematic for realistic noisy data, where systematic errors in the ΔT measurements could contaminate or bias the estimates of E- and B-mode power spectra, which have much lower magnitudes. To avoid this potential issue, we rewrite the covariance matrix in Equation (13) as:

$$\check{C}_{ij} = \langle \boldsymbol{x}_i \boldsymbol{x}_j^t \rangle = \begin{pmatrix} C^{TT} & 0 & 0 \\ 0 & C^{QQ} & C^{QU} \\ 0 & C^{UQ} & C^{UU} \end{pmatrix}. \quad (16)$$

Note that this simplification is useful only when we are interested in the polarization autospectra and do not wish to compute the polarization temperature cross-spectra. This is done by simply dropping the temperature and polarization cross covariance terms in the full covariance matrix. Therefore, we can rewrite matrices $\boldsymbol{E}_l^r$ as:

$$\check{E}^{r\ell} = \frac{1}{2} \check{C}^{-1} \frac{\partial \boldsymbol{C}}{\partial C_\ell^r} \check{C}^{-1}, \quad (17)$$

following the definition in Equation (12). The expectation values of y_l^r in Equation (11) are

$$\langle y_\ell^r \rangle = \check{F}_{\ell\ell'}^{ur} C_{\ell'}^u, \quad (18)$$

where we have used the Fisher matrix defined as:

$$\check{F}_{\ell\ell'}^{ur} = \frac{1}{2} \text{Tr} \left[\frac{\partial \boldsymbol{C}}{\partial C_{\ell'}^u} \check{C}^{-1} \frac{\partial \boldsymbol{C}}{\partial C_\ell^r} \check{C}^{-1} \right]. \quad (19)$$

Therefore, y_ℓ^r can give the unbiased estimates of the actual power spectra C_l^u with $u \in [T, E, B]$.

When we use the redefined covariance matrix of Equation (16), the power spectra estimates from relation 11 become suboptimal. However, the penalty we pay is an increase in the error bars of the power spectra estimates. It can be seen that, by redefining the covariance matrix as in Equation (16), we can separate the scalar T field from the polarization field. This allows us to only work on the QU map

for the E- and B-mode power spectra. Throughout this work, we will only work with the polarization part of the QML method. If the matrix, $\boldsymbol{F}$, is invertible, one can define unbiased estimates of the true power spectra via

$$\hat{C}_\ell^r = \check{\boldsymbol{F}}^{-1} \boldsymbol{y}^r. \quad (20)$$

The covariance matrix of the estimates y_ℓ^r is then given by:

$$\langle y_\ell^r y_{\ell'}^u \rangle - \langle y_\ell^r \rangle \langle y_{\ell'}^u \rangle \equiv F_{\ell\ell'}^{ru} = 2\,\text{Tr}[\boldsymbol{C}\check{\boldsymbol{E}}^{r\ell}\boldsymbol{C}\check{\boldsymbol{E}}^{u\ell'}], \quad (21)$$

where $\boldsymbol{F}^{ru}$ is the Fisher matrix. Thus, the covariance matrix of the true power spectra estimates of Equation (20) is given by

$$\langle \Delta \hat{C}_\ell \Delta \hat{C}_{\ell'} \rangle = \check{\boldsymbol{F}}^{-1} \boldsymbol{F} \check{\boldsymbol{F}}^{-1}. \quad (22)$$

In this work, the QML estimators have been implemented with the xQML[10] Python package (Vanneste et al. 2018).

From these equations, we observe that the computational requirements for this standard QML estimator for polarization, in its minimal form, scales as $\mathcal{O}(8N_{\text{pix, obs}}^3)$, where $N_{\text{pix, obs}}$ is the number of observed pixels. This makes the QML method for polarization computationally prohibitive beyond the lowest resolution CMB maps.

2.3. QML-SZ Estimator

In order to accelerate the computation speed of the QML estimators for CMB polarization power spectra, we introduce two new estimators. In these approaches, by applying the E–B separation methods proposed in the literature, we first construct the pure E-type or B-type polarization maps from the observed Q and U maps, which are scalar (or pseudoscalar) fields in a two-dimensional sphere. Then, we can apply the QML estimator for scalar fields (Tegmark 1997). In this article, we consider two different methods for E–B separation, which are sufficiently fast and have little information loss.

In the first approach, we consider the E–B separation method proposed in Smith (2006) and Smith & Zaldarriaga (2007). To deal with the mixture in a partial sky polarization analysis, one can construct two scalar (pseudoscalar) field quantities by using the spin-raising and spin-lowering operators (Newman & Penrose 1966), $\eth$ and $\bar{\eth}$, on $P_\pm$. Specifically, we define a new set of fields $\mathcal{E}$ and $\mathcal{B}$ as in Smith & Zaldarriaga (2007) and Zhao & Baskaran (2010):

$$\mathcal{E}(\hat{n}) = -\frac{1}{2}[\bar{\eth}\bar{\eth}P_+(\hat{n}) + \eth\eth P_-(\hat{n})], \quad (23)$$

$$\mathcal{B}(\hat{n}) = -\frac{1}{2i}[\bar{\eth}\bar{\eth}P_+(\hat{n}) - \eth\eth P_-(\hat{n})]. \quad (24)$$

These define two mutually orthogonal scalar and pseudoscalar fields, which are usually called the pure E and pure B fields in the literature. In this paper, we focus only on the B modes since the E-mode power spectrum can be recovered satisfactorily with existing estimators. Expanding the $\mathcal{B}(\hat{n})$ component in spherical harmonics, we obtain:

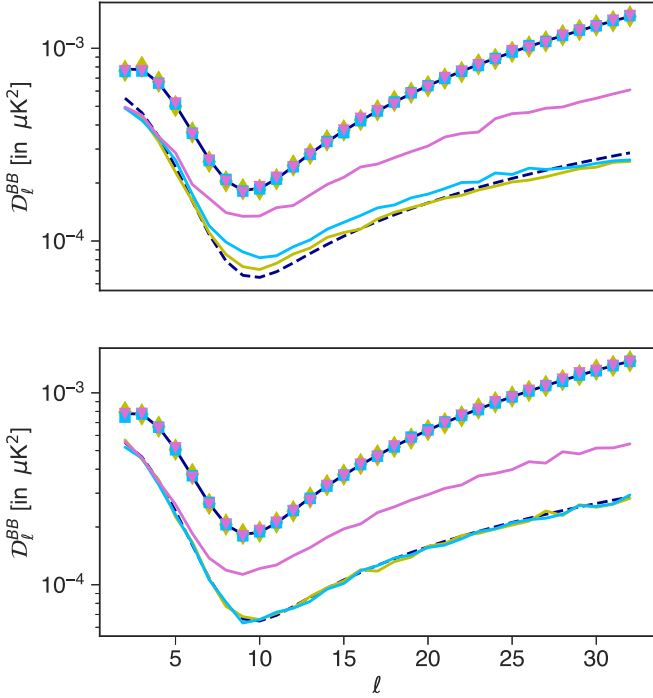$$\mathcal{B}(\hat{n}) \equiv \sum_{\ell m} \mathcal{B}_{\ell m} Y_{\ell m}(\hat{n}). \quad (25)$$

---

[10] https://gitlab.in2p3.fr/xQML/xQML

Figure 6. Plots for power spectrum reconstruction with the different QML methods with three different noise levels for the space-based experiment. The upper panel shows the QML results and the lower panels shows the QML-SZ method results. The solid black line indicates the input theoretical B-mode power spectra. The dashed black line shows the cosmic variance limit that can be obtained from Equation (50) by setting the noise to zero. We show the mean power spectra estimates with markers, and standard deviation errors with solid colored lines. The noise levels in the plot: 10 μK arcmin (pink, inverted triangle), 1 μK arcmin (cyan, square), and 0.1 μK arcmin (yellow, diamond).

The $\mathcal{B}_{\ell m}$ coefficient can then be computed from the pure B-field as:

$$\mathcal{B}_{\ell m} = \int \mathcal{B}(\hat{n}) Y_{\ell m}^*(\hat{n}) d\hat{n}. \tag{26}$$

This new pure B-mode spherical harmonic coefficient is related to the coefficient $B_{\ell m}$ as (Seljak & Zaldarriaga 1997):

$$\mathcal{B}_{\ell m} = N_{\ell,2} B_{\ell m}, \tag{27}$$

and the power spectrum becomes

$$C_\ell^{\mathcal{B}\mathcal{B}} \equiv \langle \mathcal{B}_{\ell m} \mathcal{B}_{\ell m}^* \rangle = N_{\ell,2}^2 C_\ell^{BB} \tag{28}$$

with $N_{\ell,s} = \sqrt{(\ell + s)!/(\ell - s)!}$.

For an incomplete sky observation defined by the window function $W(\hat{n})$, the partial sky harmonic coefficients of the pure E and B fields are defined as (Efstathiou 2004),

$$\tilde{\mathcal{E}}_{\ell m} = \int W(\hat{n}) \mathcal{E}(\hat{n}) Y_{\ell m}^*(\hat{n}) d\hat{n}, \tag{29}$$

$$\tilde{\mathcal{B}}_{\ell m} = \int W(\hat{n}) \mathcal{B}(\hat{n}) Y_{\ell m}^*(\hat{n}) d\hat{n}. \tag{30}$$

Following the SZ method detailed in Smith (2006), we write the partial sky pure-field harmonic coefficients as:

$$\tilde{\mathcal{E}}_{\ell m} = -\frac{1}{2} \int d\hat{n} \{ P_+(\hat{n}) [\bar{\eth}\bar{\eth}(W(\hat{n}) Y_{\ell m}(\hat{n}))]^* + P_-(\hat{n}) [\eth\eth(W(\hat{n}) Y_{\ell m}(\hat{n}))]^* \}, \tag{31}$$
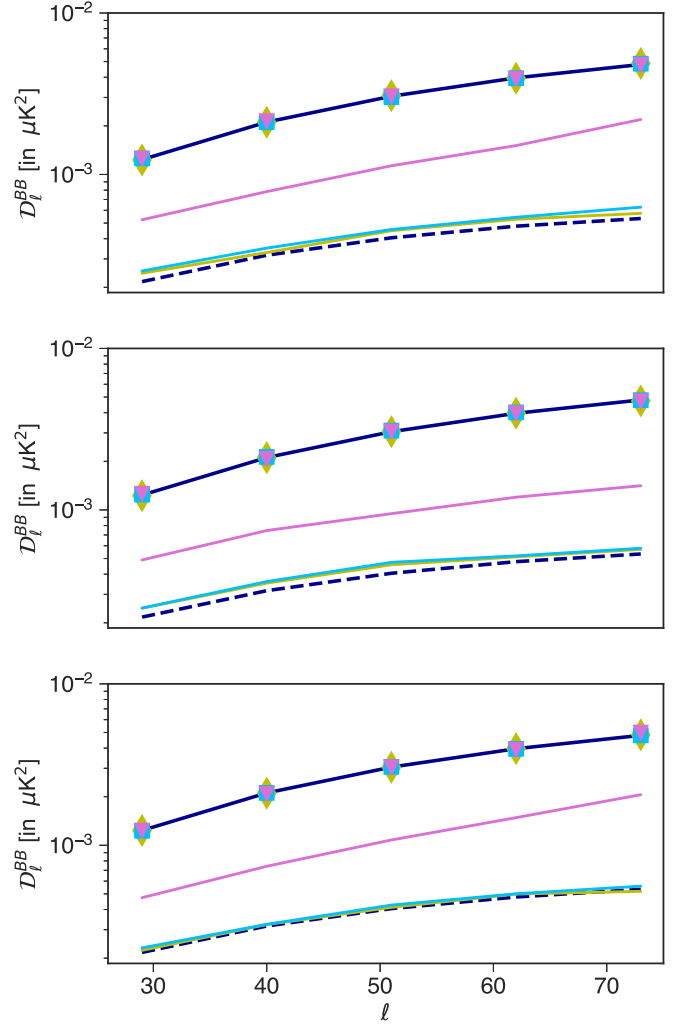
Figure 7. Plots for power spectrum reconstruction with the different QML methods with three different noise levels for the ground-based experiment. The upper panel shows the QML results, the middle panel shows the QML-SZ method results, and the lower panel shows the QML-TC method results. The solid black line indicates the input theoretical B-mode power spectra. The dashed black line shows the cosmic variance limit that can be obtained from Equation (50) by setting the noise to zero. We show the mean power spectra estimates with markers, and standard deviation errors with solid colored lines. The noise levels in the plot: 10 μK arcmin (pink, inverted triangle), 1 μK arcmin (cyan, square), and 0.1 μK arcmin (yellow, diamond).

$$\tilde{\mathcal{B}}_{\ell m} = -\frac{1}{2i} \int d\hat{n} \{ P_+(\hat{n}) [\bar{\eth}\bar{\eth}(W(\hat{n}) Y_{\ell m}(\hat{n}))]^* - P_-(\hat{n}) [\eth\eth(W(\hat{n}) Y_{\ell m}(\hat{n}))]^* \}. \tag{32}$$

These expressions can be expanded and simplified further for implementation. Full expressions can be found in Appendix A. Once the coefficients $\tilde{\mathcal{E}}_{\ell m}$ and $\tilde{\mathcal{B}}_{\ell m}$ are derived, the scalar fields in our observation window $W(\hat{n}) \mathcal{E}(\hat{n})$ and $W(\hat{n}) \mathcal{B}(\hat{n})$ can be directly obtained by inverting the relations in Equations (29) and (30).

Similar to Equation (9), the partial sky pure harmonic coefficients $\tilde{\mathcal{E}}_{\ell m}$ and $\tilde{\mathcal{B}}_{\ell m}$ are related to the full sky harmonic coefficients $E_{\ell m}$ and $B_{\ell m}$ as follows,

$$\tilde{\mathcal{E}}_{\ell m} = \sum_{\ell' m'} [\mathcal{K}_{\ell m, \ell' m'}^{EE} a_{\ell' m'}^E + i \mathcal{K}_{\ell m, \ell' m'}^{EB} a_{\ell' m'}^B], \tag{33}$$
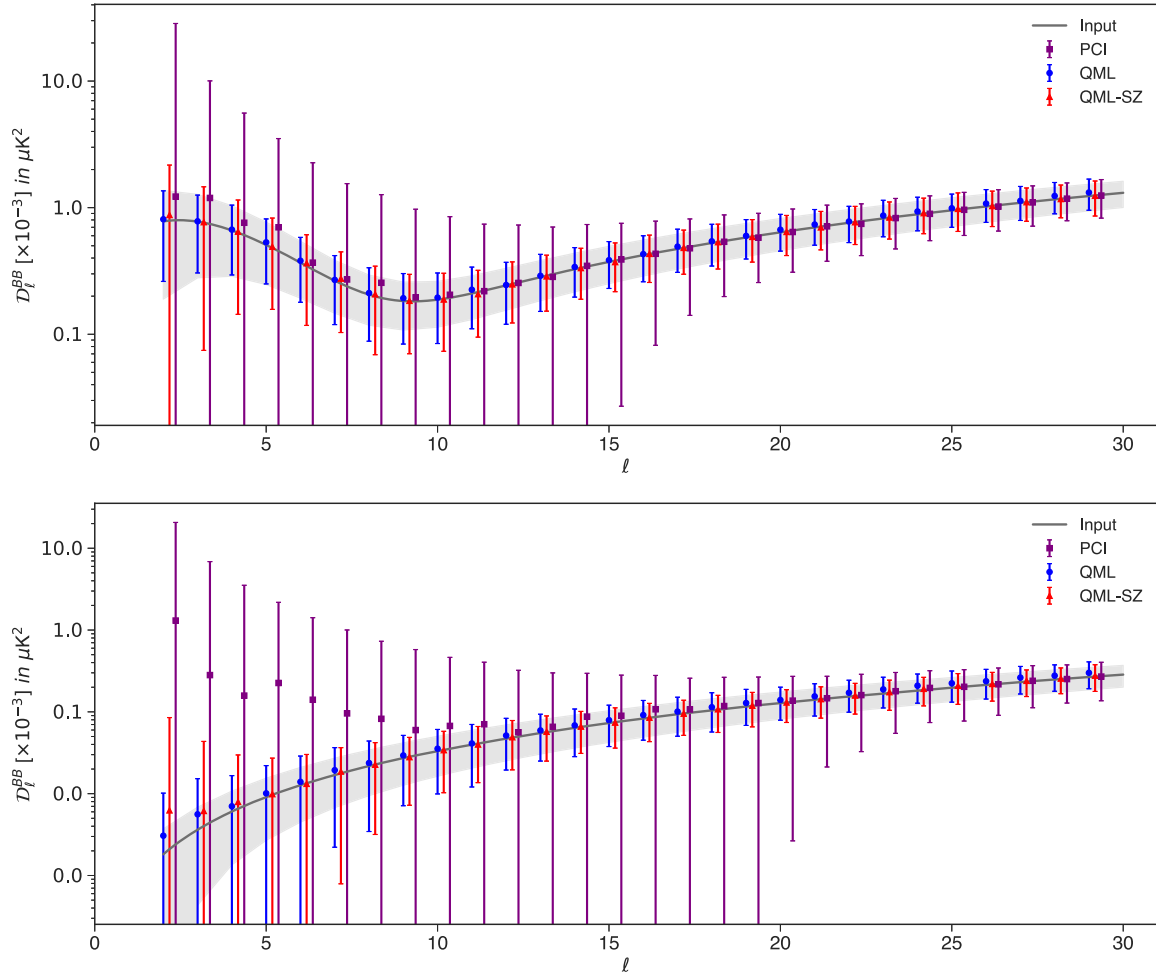
Figure 8. Plot of the results for the *B*-mode power spectrum estimates for the realistic space-based CMB experiment with $r = 0.05$ (upper panel) and $r = 0$ (lower panel), respectively. The observed sky with 3 μK arcmin noise is simulated at NSIDE = 512 with $\ell_{max} = 1024$. The input *B*-mode power spectrum is shown with the black solid curve. The classic QML method results are shown with blue, square markers, and the QML-SZ method results with red, circular markers. These results are computed at NSIDE = 16 with $\ell_{max} = 47$. We also show the PCL estimator results, obtained with NaMaster with $\delta_c = 6°$ C2 apodization, with purple, inverted triangle markers. The gray region denotes the analytical approximation of the error bounds. The data points are the mean of 1000 estimates, and the error bars are given by the standard deviation of the estimates.

$$\tilde{\mathcal{B}}_{\ell m} = \sum_{\ell' m'} [-i\mathcal{K}^{BE}_{\ell m,\ell' m'} a^E_{l' m'} + \mathcal{K}^{BB}_{\ell m,\ell' m'} a^B_{\ell' m'}], \quad (34)$$

where $\mathcal{K}^{ru}_{\ell' m' \ell m}$ are the pure-field mixing kernels, which in general can be all different, nonvanishing, and nondiagonal in both ℓ and m. Just as in the case of Equation (9), $\mathcal{K}^{EB}_{\ell' m' \ell m}$ and $\mathcal{K}^{BE}_{\ell' m' \ell m}$ are the mixing terms between the two polarization modes. However, it can be shown that for pure *E* and pure *B* construction, the mixing terms are orders of magnitude smaller than for the standard case of Equation (9). This indicates that the pure fields are nearly orthogonal with very small mixing between the two polarization modes.

In the previous subsection, the redefined covariance matrix in Equation (16) indicates that the QML estimator for the scalar temperature field can be separated from the polarization part. By using the pure *E/B* fields, we can construct the two scalar (pseudoscalar) polarization modes. Thus, it is conceivable to use the scalar QML method to estimate the power spectrum of the decoupled scalar (pseudoscalar) polarization fields. Let us briefly outline the scalar QML implementation, which we use to estimate the power spectrum of the pure *B*-field.

Let $x_i^{\mathcal{S}}$ denote the *i*th pixel value in the scalar map $x_i^{\mathcal{S}} = \mathcal{S}_i + n_i^{\mathcal{S}}$, where $n_i^{\mathcal{S}}$ is the noise in the individual pixel. The covariance matrix $C_{\mathcal{S}}$ of input data $x_i^{\mathcal{S}}$ can be written as:

$$C_{s,ij} = \langle x_i^{\mathcal{S}} (x_j^{\mathcal{S}})^t \rangle = \sum_{\ell} \frac{2\ell + 1}{4\pi} C_\ell^{SS} P_\ell(z) + N_{\mathcal{S},ij}, \quad (35)$$

where C_ℓ^{SS} means the power spectrum corresponding to the signal of scalar field map $\mathcal{S}(\hat{n})$ and $N_{\mathcal{S}}$ is the noise variance matrix.

According to the QML approach, we can construct the optimal estimator by making use of $C_{S,ij}$ and $x_i^{\mathcal{S}}$,

$$y_\ell^{\mathcal{S}} = x_i^{\mathcal{S}} x_j^{\mathcal{S}} E_{\mathcal{S},ij}^\ell - b_\ell^{\mathcal{S}}. \quad (36)$$

The matrices $E_{\mathcal{S}}^\ell$ have a similar form to Equation (12)

$$E_{\mathcal{S}}^\ell = \frac{1}{2} C_{\mathcal{S}}^{-1} \frac{\partial C_{\mathcal{S}}}{\partial C_{\mathcal{S},\ell}} C_{\mathcal{S}}^{-1}. \quad (37)$$
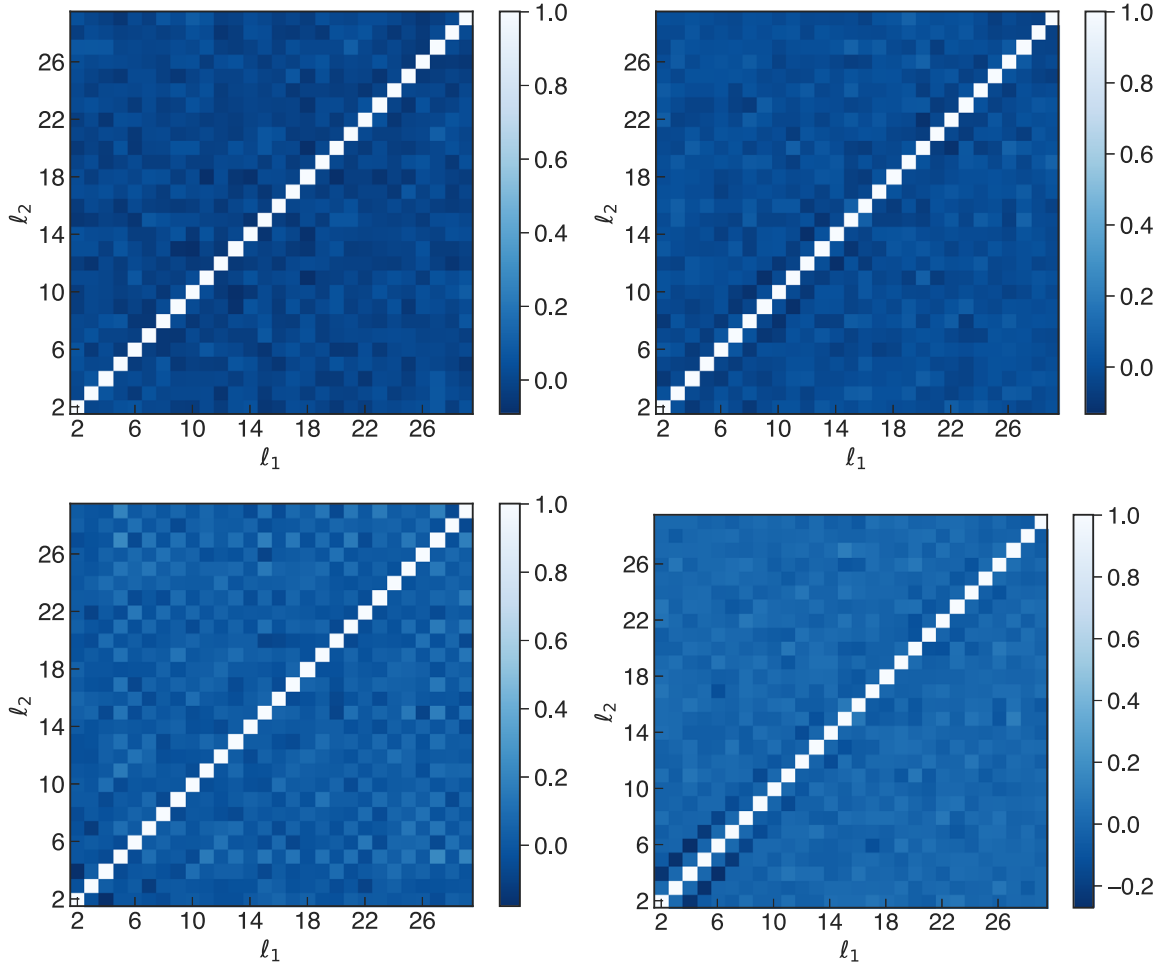
Figure 9. Normalized covariance matrices $\mathcal{C}_{\ell,\ell'} = \mathrm{cov}(\hat{C}_\ell, \hat{C}_{\ell'})/\sqrt{\mathrm{var}(\hat{C}_\ell)\,\mathrm{var}(\hat{C}_{\ell'})}$ of the three QML methods for the space-based experiment. The matrices are obtained from estimates of 1000 simulations for the classic QML estimator (left) and for QML-SZ estimator (right). The upper diagrams show the covariance matrices of the $r = 0.05$ case, and the lower diagrams show equivalent plots for the $r = 0$ case.

Similarly, the Fisher matrix $F_{S,\ell\ell'}$ expression becomes:

$$F_{S,\ell\ell'} = \frac{1}{2} Tr\left[\frac{\partial \boldsymbol{C}_{\mathcal{S}}}{\partial C_{\mathcal{S},\ell}}\boldsymbol{C}_{\mathcal{S}}^{-1}\frac{\partial \boldsymbol{C}_{\mathcal{S}}}{\partial C_{\mathcal{S},\ell'}}\boldsymbol{C}_{\mathcal{S}}^{-1}\right]. \quad (38)$$

The QML estimator for a scalar power spectrum $\hat{C}_\ell^{\mathcal{S}\mathcal{S}}$ is given by

$$\hat{C}_\ell^{\mathcal{S}\mathcal{S}} = (\tilde{\boldsymbol{F}}_{\mathcal{S}})^{-1}\boldsymbol{y}^{\mathcal{S}}. \quad (39)$$

We apply this scalar QML method to estimate the power spectrum of the decoupled pure B polarization field, and it is denoted as the QML-SZ estimator in this work.

In the SZ approach to separate the E and B modes, we must use a proper sky apodization, instead of the binary window function, to avoid numerical divergences in the calculation of the window function derivatives. A Gaussian smoothing kernel has been shown to induce very small leakage in the final B map (Wang et al. 2016; Kim 2011). So, this is our apodization choice for obtaining the pure B map for the QML-SZ method. For the ith pixel in the region allowed by the binary mask, the

apodized window is defined as:

$$W_i = \begin{cases} \frac{1}{2} + \frac{1}{2}\mathrm{erf}\left(\frac{\delta_i - \frac{\delta_c}{2}}{\sqrt{2}\,\sigma}\right), & \delta_i < \delta_c \\ 1, & \delta_i > \delta_c \end{cases} \quad (40)$$

where δ_i is the shortest distance between the ith observed pixel from the boundary of the allowed region, $\sigma = \mathrm{FWHM}/\sqrt{8\ln 2}$ with FWHM denoting the full width at half maximum of the Gaussian kernel, and δ_c is the apodization length which acts as an additional adjustable parameter.

Now, we summarize the construction of the QML-SZ estimator as follows. For the given observed Q and U polarization maps, we construct a partial sky pure B-type map $\mathcal{B}(\hat{n})$, following the SZ method with Gaussian apodization of the binary window function. Then, we use the $\mathcal{B}(\hat{n})$ map and $C_\ell^{\mathcal{B}\mathcal{B}}$ as input parameters to replace $x_i^{\mathcal{S}}$ and $C_\ell^{\mathcal{S}\mathcal{S}}$ in the scalar QML method to estimate the B-mode power spectrum C_ℓ^{BB}. In comparison with traditional QML estimator, our goal with the QML-SZ method is to simplify the calculation, without compromising significantly on the accuracy or error bars. We
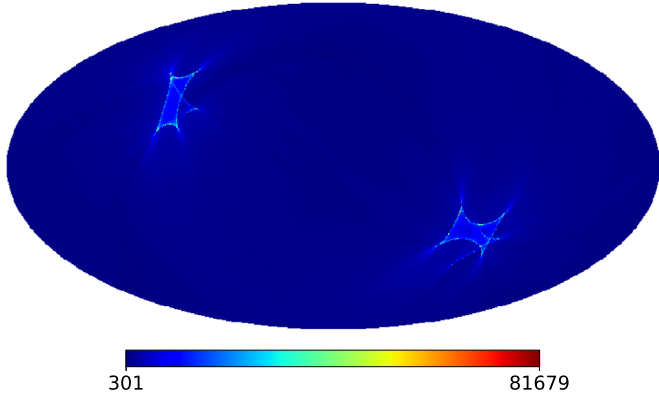
Figure 10. A hitmap in Galactic coordinates of the Planck 100 GHz channel, obtained for `NSIDE = 2048`. Pixel values quantify the number of observations of the pixel. Areas near the ecliptic poles are observed several times more frequently than regions of the sky near the ecliptic plane. The lowest values are about 301 while the highest are about 8.2×10^4.

implement the QML-SZ estimator with the modified xQML Python package.

2.4. QML-TC Estimator

In this subsection, we describe a similar procedure to construct a B-mode map that is leakage free, and then use the scalar QML method to estimate the power spectrum. We use the E-mode recycling method proposed in Liu et al. (2019a, 2019b) to obtain a leakage free B-mode map. This procedure essentially uses the E-mode signal in the CMB map to estimate the leakage due to the incompleteness of the sky. This template for the leakage is then used to clean the B-mode map. The mathematical principle of this idea is the following:

The true E-to-B leakage in the pixel domain is given by the following equation:

$$L(\boldsymbol{n})_{\text{true}} = \int G_{EB}(\boldsymbol{n}, \boldsymbol{n}')\boldsymbol{P}(\boldsymbol{n}')d\boldsymbol{n}', \qquad (41)$$

where $G_{EB}(\boldsymbol{n}, \boldsymbol{n}')$ is the convolution kernel of the E-to-B leakage given in Equation (3.2) of Liu et al. (2019b), and $\boldsymbol{P}(\boldsymbol{n}')$ includes both the Q and U Stokes parameters. Note that this convolution kernel is fixed and does not change with different realizations of the CMB sky.

The above integral should be calculated over the entire sphere. This explains why the true E-to-B leakage cannot be precisely estimated in the case of partial sky coverage. However, the above equation also tells us that if there is no additional information regarding the mission's sky region, then the estimation of the E-to-B leakage is given by

$$L(\boldsymbol{n})_{\text{blind}} = \int G_{EB}(\boldsymbol{n}, \boldsymbol{n}')\boldsymbol{P}(\boldsymbol{n}')M(\boldsymbol{n}')d\boldsymbol{n}', \qquad (42)$$

where $M(\boldsymbol{n}')$ is the sky mask. The above equation can be further decomposed into the combination of two integrals:

$$L(\boldsymbol{n})_{\text{blind}} = \int G_B(\boldsymbol{n}, \boldsymbol{n}')M(\boldsymbol{n}')d\boldsymbol{n}'$$
$$\int G_E(\boldsymbol{n}', \boldsymbol{n}'')M(\boldsymbol{n}'')\boldsymbol{P}(\boldsymbol{n}'')d\boldsymbol{n}'', \qquad (43)$$

where $G_E(\boldsymbol{n}, \boldsymbol{n}')$ and $G_B(\boldsymbol{n}, \boldsymbol{n}')$ are the pixel domain convolution kernels of the E- and B-mode signals, respectively. Mathematically, the integrals with these two kernels are

nothing but standard forward-backward spherical harmonic transforms of the E and B modes.

Therefore, the algorithm for the template cleaning method is:

1. Starting with the data vector $\boldsymbol{x}$ from Equation (10) and the binary window function for the observed sky W, we obtain the spherical harmonic coefficients $a_{\ell m}^r$ with $r \in [T, E, B]$.
2. We reconstruct a QU map with the $a_{\ell m}^E$s only. In the CMB case, the power in the B mode is much smaller than that in the E-mode. So, compared to the E-mode signal, the leakage from B-to-E is negligible. Therefore, this QU map represents the actual E-mode-only CMB polarization in the observed sky patch.
3. Next, we mask the E-mode-only QU maps again with the binary window function and obtain harmonic coefficients $\bar{a}_{\ell m}^r$, with $r \in [E, B]$. Since these QU maps were constructed from only E-mode information, any B modes generated by the harmonic transformation is produced by the E-to-B leakage. So we can construct a scalar B-mode leakage template by using the $\bar{a}_{\ell m}^B$ obtained this way.
4. We use the original $a_{\ell m}^B$ to obtain a scalar B-mode map, which is contaminated by E-to-B leakage. With the contaminated B-mode map, we can obtain a linear fit of the leakage template, which is subtracted from the contaminated B-mode map in pixel space to obtain the leakage cleaned B map.

This cleaned B map is essentially the isolated B-mode pseudoscalar field, and we can apply the scalar QML estimator to reconstruct its power spectrum. However, the template cleaning method is not perfect so we will have some residual leakage that gets left in the cleaned B maps. Therefore, the cleaned B map can be treated as $B_i + x_i^R + n_i^B$, where B_i is the ith pixel value of the cleaned B modes, x_i^R is the residual leakage, and n_i^B is the noise. This residual leakage term will be treated similar to the noise contribution. In practice, we compute the residual leakage covariance matrix from simulations. Then the scalar covariance matrix shown in Equation (35) becomes:

$$C_{B,ij} = \langle x_i^B(x_j^B)^t \rangle = \sum_\ell \frac{2\ell + 1}{4\pi} C_\ell^{BB} P_\ell(z) + N_{ij} + R_{ij}, \quad (44)$$

where R_{ij} is the covariance matrix of residual leakage.

The bias term b_ℓ^B is now given by $Tr[\boldsymbol{E}_\ell(\boldsymbol{N} + \boldsymbol{R})]$. We find that, for $\ell > 5$, the impact of the residual leakage can be removed by masking pixels near the mask boundary in the cleaned B map, and its impact on the final results can be ignored in most cases. In this paper, we mask all pixels 3°.5 from the mask boundary. The results of the QML methods discussed here are also not very sensitive to the choice of the fiducial C_ℓ^{BB} or C_ℓ^{BB} chosen in computing the signal covariance matrix. For example, a different choice of the tensor-to-scalar ratio does not make any difference in the final results.

Using the template cleaned B-mode map as input and the covariance matrix above, we use the scalar QML (Equations (37) to (39)) to obtain the QML-TC estimator for the B-mode power spectrum. Similar to the QML-SZ estimator, the QML-TC estimator is a much simpler implementation that should have reasonably good performance at the largest scales. In our calculation, the QML-TC estimator is also implemented with the xQML Python package.
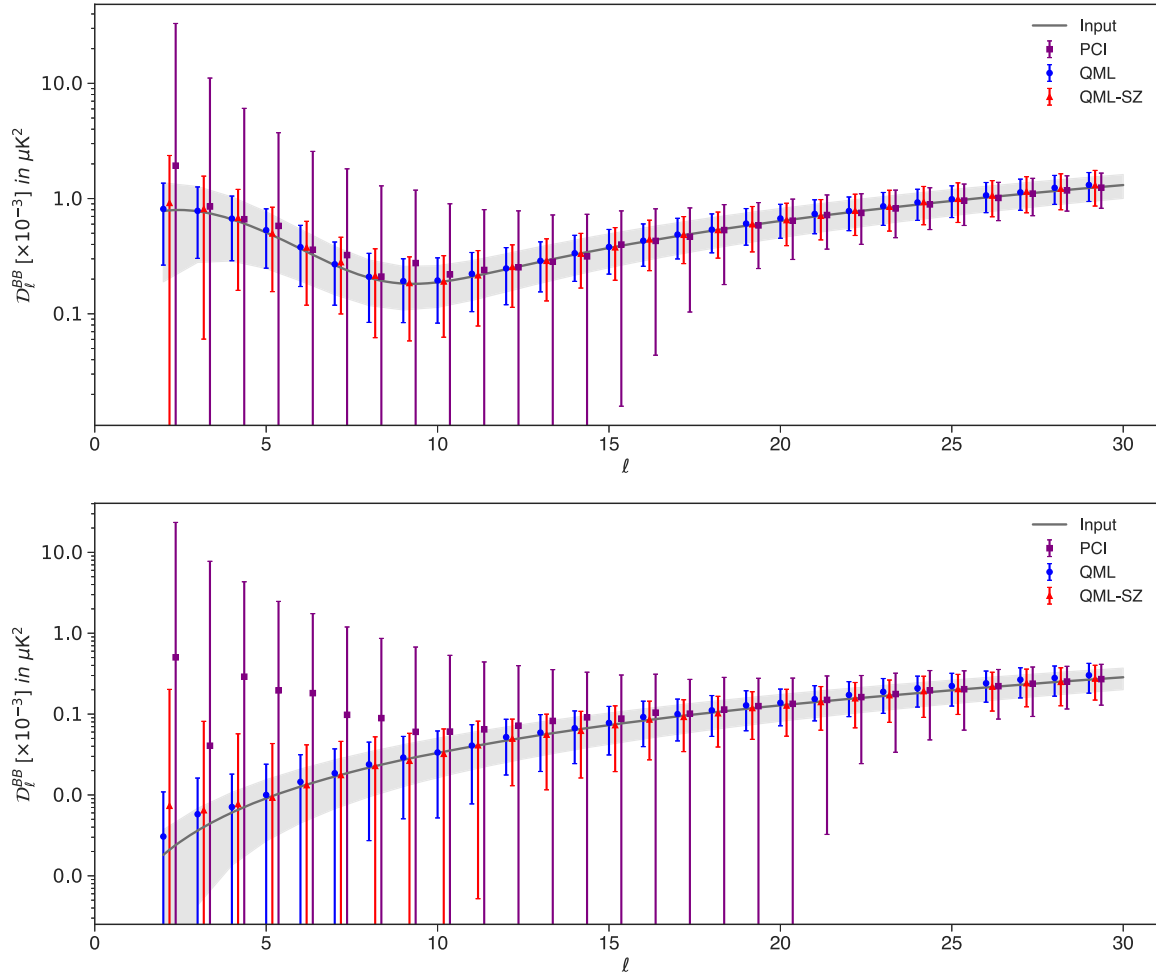
Figure 11. Plot of the results for B-mode power spectrum estimates for the realistic space-based CMB experiment for $r = 0.05$ (upper panel) and $r = 0$ (lower panel), respectively. The observed sky with inhomogeneous noise is simulated at NSIDE = 512 with $\ell_{max} = 1024$. The input B-mode power spectrum is shown with the black solid curve. The classic QML method results are shown with blue, square markers, and the QML-SZ method results with red, circular markers. These results are computed at NSIDE = 16 with $\ell_{max} = 47$. We also show the PCL estimator results, obtained with NaMaster with $\delta_c = 6°$ C2 apodization, with purple, inverted triangle markers. The gray region denotes the analytical approximation of the error bounds. The data points are the mean of 1000 estimates, and the error bars are given by the standard deviation of the estimates.

2.5. Pure B-mode PCL Estimator

The most common method that is adopted in CMB data analysis is the so-called pseudo-C_ℓ (PCL) estimators, which are both computationally inexpensive and near optimal at high multipoles. For polarization analysis with PCL estimators, the preferred method is to work with pure E and pure B fields. In case of an incomplete sky, Equations (33) and (34) give the relation between the partial sky pure E/B-mode harmonics and the full sky E and B modes. They can be used to obtain a relation between the partial sky pure E/B power spectra and the actual E/B-mode power spectra:

$$\tilde{C}_\ell^{\mathcal{EE}} = \sum_{\ell'}[\mathcal{M}_{\ell\ell'}^{EE} C_{\ell'}^{EE} + \mathcal{M}_{\ell\ell'}^{EB} C_{\ell'}^{BB}], \tag{45}$$

$$\tilde{C}_\ell^{\mathcal{BB}} = \sum_{\ell'}[\mathcal{M}_{\ell\ell'}^{BE} C_{\ell'}^{EE} + \mathcal{M}_{\ell\ell'}^{BB} C_{\ell'}^{BB}]. \tag{46}$$

In these expressions $\mathcal{M}_{\ell\ell'}^{ru}$ is the mixing matrix that relates the two sets of power spectra. The mixing matrices are defined as:

$$\mathcal{M}_{\ell\ell'}^{ru} = \frac{1}{2\ell + 1}\sum_{mm'}|\mathcal{K}_{\ell m\ell'm'}^{ru}|^2, \tag{47}$$

with $r, u \in [E, B]$. The exact expressions for the mixing matrices can be found in Grain et al. (2009). We can solve the set of Equations (45) and (46) for the E- and B-mode power spectra. These are called the pseudo-full-sky power spectra estimates. In this work, we will compare the performance of the three QML methods with the PCL method in the multipole range of interest.

When we perform a spherical harmonic transformation with binary window functions, it will lead to severe leakage and mode mixing. Therefore we have apodized our observation window with a "C2" (cosine) apodization function for the PCL estimates in this work. The weight in the ith pixel is given as (Alonso et al. 2019):

$$\begin{cases} W_i = \frac{1}{2}[1 - \cos(\pi\delta_i^r)] & \delta_i^r < 1 \\ 1 & \text{otherwise,} \end{cases} \tag{48}$$

where $\delta_i^r = \sqrt{(1 - \cos\delta_i)/(1 - \cos\delta_c)}$. We compute all PCL estimator results in this work with the C2 apodization. The PCL estimator for this work has been implemented with the Python package of NaMaster[11] (Alonso et al. 2019).
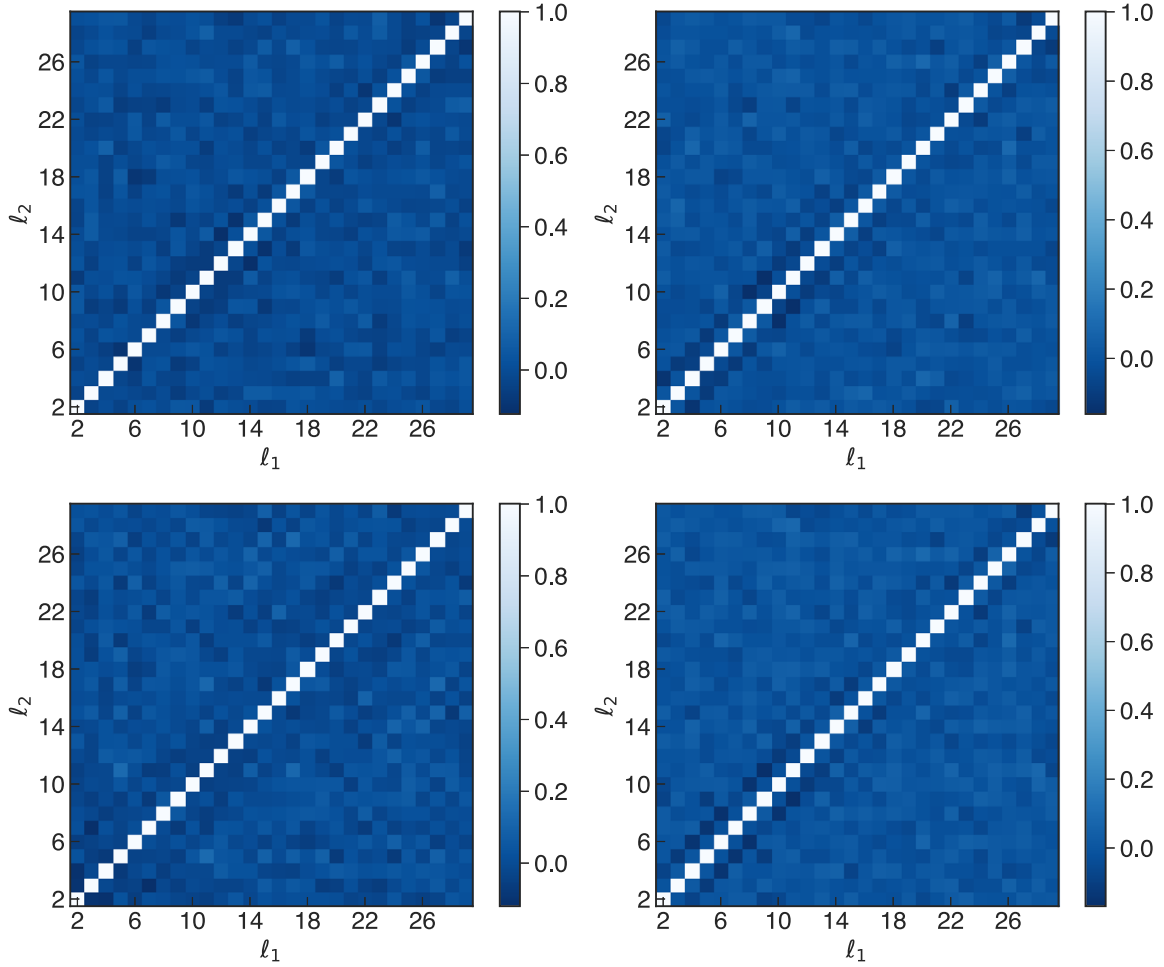
---

[11] https://github.com/LSSTDESC/NaMaster

Figure 12. Normalized covariance matrices $\mathcal{C}_{\ell,\ell'} = \mathrm{cov}(\hat{C}_\ell, \hat{C}_{\ell'}) / \sqrt{\mathrm{var}(\hat{C}_\ell)\,\mathrm{var}(\hat{C}_{\ell'})}$ of the three QML methods for the space-based experiment with inhomogeneous noise. The matrices are obtained from estimates of 1000 simulations for the classic QML estimator (left) and for the QML-SZ estimator (right). The upper diagrams show the covariance matrices of the $r = 0.05$ case and the lower diagrams show equivalent plots for the $r = 0$ case.

3. Simulation Setup and Idealized Tests

In this work, we consider two cases of future CMB polarization experiments: a space-based experiment and a ground-based polarization experiment. In both cases, due to astrophysical foreground and/or survey limitations, only an incomplete sky patch can be used for scientific analysis. Thus, for each experimental scenario the E-to-B leakage is going to be a challenge. For the space-based experiment case, we consider the 2018 Planck common polarization mask, which masks the Galactic foregrounds and the point sources resolved in Planck maps. Using the HEALPix `process_mask` subroutine we fill in all of the point sources smaller than $5°$ that are masked, as well as the extended source masking at high Galactic latitudes ($|b| > 45°$). We assume this is the observed sky patch with $f_{\rm sky} \sim 78.8\%$, which is representative of a space-based polarization experiment. In addition, we consider an $f_{\rm sky} \sim 15.1\%$ sky patch in the northern hemisphere, based on the AliCPT-1 experiment (Li et al. 2017; Salatino et al. 2021), for the observed sky of the ground-based experiment simulations. We show the binary mask for these two sky patches in Figure 1.

In our calculation, the CMB map simulations are produced using the `synfast` subroutine of HEALPix[12] with the input

CMB power spectra generated by CAMB[13] (Lewis et al. 2000). In this article, we consider the 2018 Planck cosmological parameters (Planck Collaboration et al. 2020), including weak lensing contributions, and setting the tensor-to-scalar ratio r to 0.05. For the realistic examples shown in Section 4, we additionally compute the results for $r = 0$. The choices for the tensor-to-scalar ratio denote the current upper and lower limits on the value of r (BICEP2/Keck Collaboration et al. 2015).

Before considering realistic simulations to test the performance of the three estimators, we first perform some idealized tests to identify the impact on the results of various factors of our simulation setup. These analyses independently take into account the effects due to masking, the downgrading procedure, and different white noise levels. For optimizing our simulation pipeline considering these idealized tests, we use full sky maps. Therefore, we do not produce scalar maps of pure B or template cleaned B-mode maps from masked TQU maps, in order to prevent any additional complications that might arise from any residual E-to-B leakage in the scalar maps. In summary, we simulate a full TQU CMB map in order to test the optimal simulation settings for the standard QML method. We simulate a scalar pure B map, $\mathcal{B}(\hat{n})$, with $C_\ell^{\mathcal{BB}}$ as
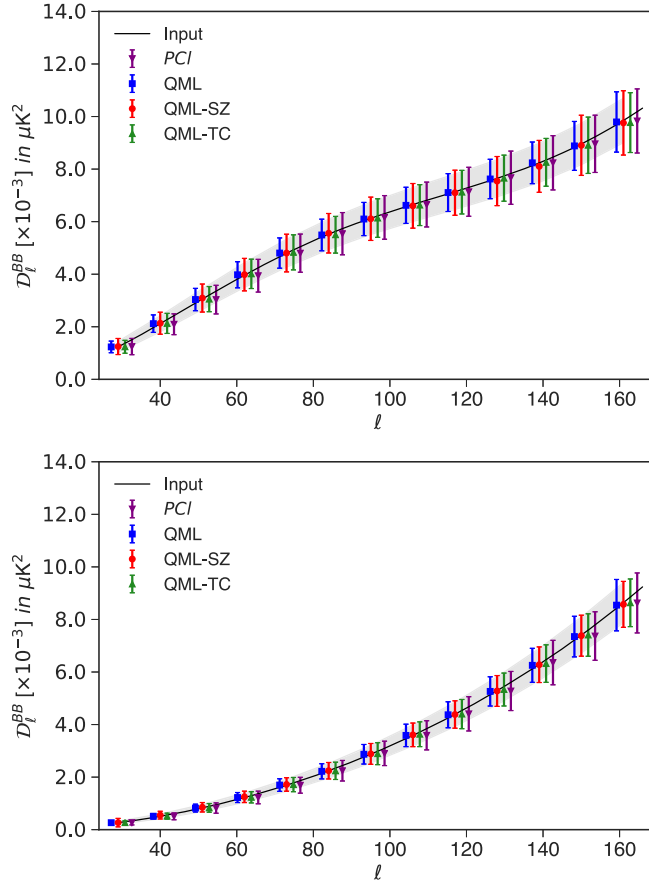

Figure 13. Plot of the results of *B*-mode power spectrum estimates for a realistic ground-based CMB experiment with homogeneous noise, for $r = 0.05$ (upper panel) and $r = 0$ (lower panel), respectively. The observed sky with 3 μK arcmin noise is simulated at NSIDE = 512 with $\ell_{max} = 1024$. The input *B*-mode power spectrum is shown with the solid, black curve. The classic QML method results are computed at NSIDE = 64 with $\ell_{max} = 192$ (blue, square markers), the QML-SZ method results are computed at NSIDE = 64 with $\ell_{max} = 192$ (red, circle markers), and the QML-TC method results are also computed at NSIDE = 64 with $\ell_{max} = 192$ (green, triangle markers). We also show the PCL estimator results, obtained with NaMaster using $\delta_c = 6°$ for $r = 0.05$ and $\delta_c = 10°$ for $r = 0$ (purple, inverted triangle markers). The gray region denotes the optimal error bounds. The data points are mean of 1000 estimates and the error bar is given by the standard deviation of the estimators.

input to optimize the QML-SZ estimator, and, finally, for the QML-TC estimator, we simulate a scalar *B*-mode map with input C_ℓ^{BB}.

The computational requirement for a QML method scales with the size of the data vector $\boldsymbol{x}$. For the full standard QML method with temperature and polarization, the size of data vector N_d is $3 \times N_{\text{pix, obs}}$, where $N_{\text{pix, obs}}$ is the number of pixels in the observed sky patch. However, as described in Section 2.2, we will work with only the polarization part of the QML estimator. This reduces the size of the data vector to $2 \times N_{\text{pix, obs}}$ by dropping the *T* fields. For both of the scalar methods, the data vector size is $N_d = N_{\text{pix, obs}}$. The size of the computational requirement is set by the size of the covariance matrix, which is $N_d \times N_d$. The inversion of the covariance matrix is therefore an $O(N_d^3)$ operation. Thus, the scalar QML method has a significant advantage regarding memory and computation time required in the estimation. This is also a limiting factor for the HEALPix map resolution we can work with for a given experiment. For the space-based experiment, since the observed sky fraction is quite large, we work at NSIDE = 16, with $\ell_{max} = 2 \times$NSIDE. But for the small sky patch of the ground-based experiment, we can choose a higher resolution of NSIDE = 32, with $\ell_{max} = 3 \times$NSIDE.

Unfortunately, the template cleaning method has residuals that impact the power spectrum estimation at the lowest multipoles. Therefore, in the satellite case, we will not consider the QML-TC estimator, since, in this particular case, we expect accurate estimation even in lowest multipoles. We discuss this issue in more detail in Appendix B.

3.1. Effect of f_{sky}

In an incomplete sky, besides the mixtures between the *E* and *B* modes, we have to deal with the well-known mode mixing problem. In this subsection, we will test the QML estimator, as well as the QML-SZ and QML-TC estimators, introduced previously. As discussed, we simulate the pure *B* and *B*-mode maps directly from $C_\ell^{\mathcal{B}\mathcal{B}}$ and C_ℓ^{BB}, so there is no *E*-to-*B* leakage residual contribution. We simulate at NSIDE of 16 and 32 for satellite and ground experiments, respectively, with the noise level set to 0.1 μK arcmin, which is close to the noise-free case. Therefore, we can only study the effect of mode mixture caused by the partial sky surveys.

In Figures 2 and 3, we show the power spectra estimates plotted for space-based and ground-based experiments, respectively. Note that we have binned the power spectra with the
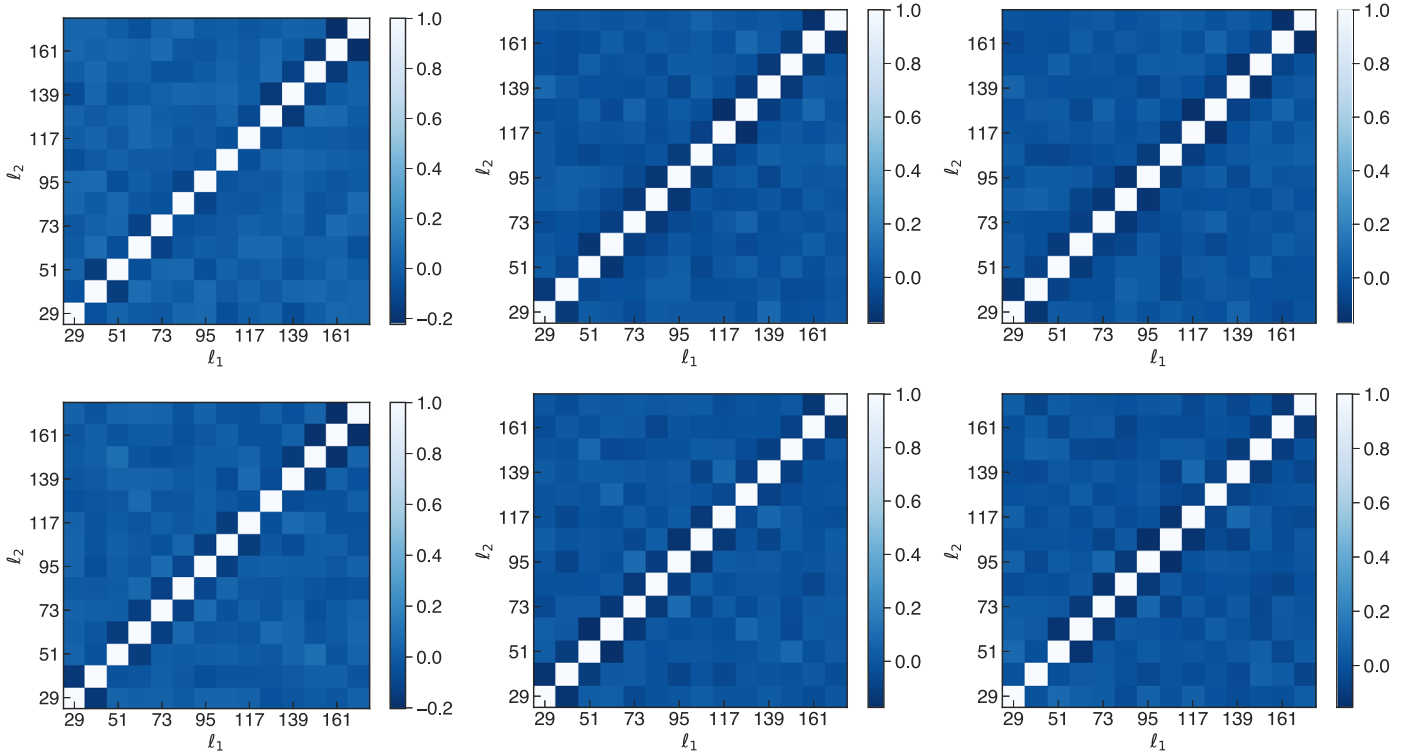
Figure 14. Binned normalized covariance matrices $\mathcal{C}_{\ell,\ell'} = \mathrm{cov}(\hat{C}_\ell, \hat{C}_{\ell'})/\sqrt{\mathrm{var}(\hat{C}_\ell)\mathrm{var}(\hat{C}_{\ell'})}$ of the three QML methods for the ground-based experiment, with homogeneous noise. The upper diagrams show the covariance matrix for the $r = 0.05$ case and the lower diagrams show the covariance matrix for the $r = 0$ case. The matrices are obtained from estimates of 1000 simulations for the classic QML estimators (left), the QML-SZ estimators (center), and the QML-TC estimators (right).

following definition,

$$\mathcal{D}_\ell^{BB} = \frac{1}{\Delta\ell} \sum_{\ell'=\ell-\Delta\ell/2}^{\ell'=\ell+\Delta\ell/2} \frac{\ell'(\ell'+1)}{2\pi} C_{\ell'}^{BB}, \qquad (49)$$

where $\Delta\ell$ is the bin width. For the space-based experiment, due the large sky coverage, it is reasonable to estimate the power spectra at each multipole, hence we set $\Delta\ell = 1$. For ground-based experiments, we bin the power spectrum into bands with $\Delta\ell = 11$ to mitigate the greater mode mixing problem due to a smaller observation patch. Throughout this work, our power spectra estimates for any estimator is a mean of 1000 random simulations, and the errors are computed as the standard deviation of the samples. For comparison, we also compare our results with the simple analytical estimate of error bars, which is given by

$$\Delta\mathcal{D}_{\ell,\mathrm{optimal}}^{BB} \cong \sqrt{\frac{2}{(2\ell+1)\Delta\ell f_{\mathrm{sky}}}} [\mathcal{D}_\ell^{BB} + \mathcal{N}_\ell^{BB}], \qquad (50)$$

where $\mathcal{N}_\ell^{BB}$ is the noise power spectrum binned using relation (49).

As anticipated, the results in Figures 2 and 3 show that all three methods can obtain unbiased estimates for the B-mode power spectrum. Next, we will investigate the impact of f_{sky} on the error bars. In the case of the Planck mask, we find the rms errors of these QML methods are even smaller than for the analytical results in Equation (50), since the large-scale information in the masked region can be partly recovered by the QML analysis, which is consistent with the results in Efstathiou (2004, 2006). For smaller scales, the errors of the

three methods are optimal, and all methods perform equally. Our results show that the mode mixing due to f_{sky} is sufficiently well corrected in all of the presented methods, and its impact on the final results is negligible for both of the two sky patches considered in this work.

3.2. Impact of Downgrading the Map

Actual CMB polarization maps are usually at much higher resolution than the resolution imposed by computational limitations in calculating the QML estimator. Any analysis using QML estimators will then require a smoothing process to reduce the influence of higher multipoles, followed by a downgrading process to reduce the NSIDE of the map. The map degrading process for this work will be done with the ud_grade subroutine from HEALPix. In this subsection, we test the impact of ud_grade alone (without considering the effect of smoothing).

For this test, we simulate CMB maps at NSIDE = 512, with ℓ_{max} set to 32 and 96 for the space-based and ground-based cases, respectively. This is done to mimic the cases with smoothing that cuts off the modes above the set ℓ_{max} values. Thus, it helps to isolate the effect of the downgrading procedure only. The full sky maps at NSIDE = 512 are masked with appropriate binary masks and then downgraded to the targeted NSIDE by ud_grade. We also downgrade the masks with ud_grade and set any pixels with values <0.99 to zero. We multiply this downgraded mask by the downgraded maps, which act as the input maps for the QML estimators.

The results for the impact of ud_grade are shown in Figures 4 and 5 for the space-based and ground-based experiment cases, respectively. For both sky patches, we find
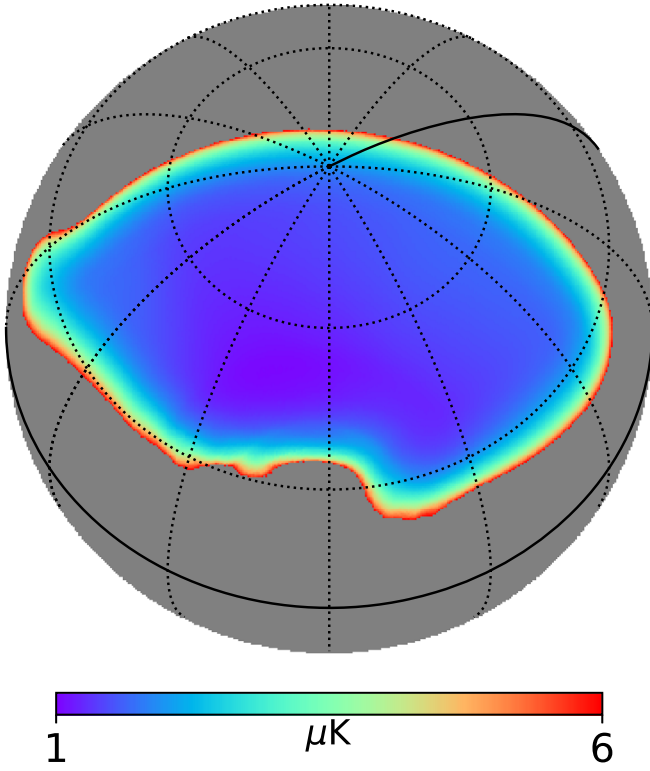
Figure 15. Map for the standard deviation of noise per pixel (in unit of μK) for the AliCPT 95 GHz channel for one possible scan strategy.

that downgrading the map has a negligible impact on the mean estimates. Thus, this process does not generate any additional biases to the QML estimators. For the space-based experiment case, the error bars for $\ell \leqslant 5$ show a small increase for the QML estimator and a significant increase for the QML-SZ estimator. This behavior can be explained by the power spectrum of QML-SZ method, which is given by $N_{\ell,2}^2 C_\ell^{BB}$. By downgrading the map, the power from high multipoles leaks to the lower multipoles and increases the uncertainty on the large angular scales. We also find that errors for the standard QML estimator slightly increase throughout the multipole range, though the errors are still near optimal. For the ground-based experiment, we find a negligible impact of the downgrading process on the error bars.

3.3. Impact of Noise Level

In every CMB experiment, we have to suitably mitigate the impact of the noise. The noise level depends on various factors, such as instrument sensitivity, survey duration, survey strategy, etc. As mentioned before, the rms noise levels can vary due to various factors, but for this work we test three cases: 10 μK arcmin, 1 μK arcmin, and 0.1 μK arcmin, the latter one acting as the noise-free limit of our estimator performance.

For this study, we simulated the different noise maps at the targeted NSIDE = 16 for the large sky fraction patch and NSIDE = 32 for the small sky patch. The rms noise levels are suitably converted to get the noise variance per pixel at one of those NSIDE values. This is used to generate Gaussian white noise. The CMB maps are simulated at the targeted NSIDE with $\ell_{\max}$ of 32 and 96. The two maps are then coadded and masked to produce the input maps for the QML estimators.

In Figures 6 and 7, we show the results for the power spectra estimated with the QML methods for the large and small sky fraction patches. In these figures, we compare the errors with the cosmic variance limit that can be obtained from Equation (50) by setting $\mathcal{N}_\ell^{BB}$ to zero. We can see that the variation in the noise level does not affect the mean of the power spectra estimates. This is expected as we have the b_ℓ^r term in Equation (11) to debias for the noise. We also find that the noise level will impact the error bars, but at a low noise level it almost behaves as the cosmic variance limited case. Considering the same noise level, for every tested case, all of the QML estimators behave very similar to each other.

4. Realistic Examples

In the previous section, we have performed some idealized tests for three QML estimators. In this section, we consider more realistic simulations, which show a precise implementation of the pipeline to obtain the power spectrum estimates from CMB observations with all three estimators. Finally, we will obtain a detailed comparison of the computational requirements for these three methods. Here, we are comparing the performance of our estimators in four situations: satellite- and ground-based experiments, both with homogeneous noise and inhomogeneous noise.

To simulate the CMB sky, we use the 2018 Planck cosmological parameters as given by the Planck Collaboration et al. (2020) for the E-mode input signal. For the B-mode input signal, we include lensing and primordial B modes with both $r = 0.05$ and $r = 0$, which represent the upper and lower limits on r.

Here, we will outline the common simulation setup for our realistic examples. We simulate full sky CMB realizations at NSIDE = 512 with $\ell_{\max} = 1024$ for both $r = 0.05$ and $r = 0$ by using the synfast subroutine of HEALPix. To simulate the noise map, we consider two different cases. For the homogeneous noise case, the rms white noise level for our realistic examples is set to 3 μK arcmin. This equates to a white noise level of 0.44 μK pixel at NSIDE = 512. We simulate Gaussian white noise at NSIDE = 512 on full sky. For the inhomogeneous noise case, we use different ways to generate noise maps for the space-based and ground-based experiments (see Sections 4.2 and 4.4 for details). The signal and noise maps are finally coadded to generate our "observed" CMB map.

In the satellite-based experiment case, we use the HEALPix smoothing subroutine to smooth the "observed" CMB map with FWHM = 8° to suppress higher multipoles. While, for the ground-based experiment, the coadded maps are multiplied by a particular binary mask (see Figure 1) to keep only the fraction of sky observed in the considered experiment. This produces our simulated CMB observations from the two experimental setups considered.

In the next step, we first need to prepare our scalar pure B map, $\mathcal{B}(\hat{n})$, at NSIDE = 512 by using a Gaussian apodized mask with $\sigma = 10^{-6}$, $\delta_c = 1°$ for the Planck mask and $\sigma = 10^{-4}$, $\delta_c = 0.5°$ for the AliCPT mask in Equation (40). We use the expression (A5) for this computation. Similarly, we use the template cleaning algorithm detailed in Section 2.4 to produce a leakage template cleaned scalar B-mode map. Thus, we derive TQU maps for the QML method, a scalar $\mathcal{B}$ map for the QML-SZ method, and a template cleaned B map for the QML-TC method. As we have discussed in Section 2.5, we
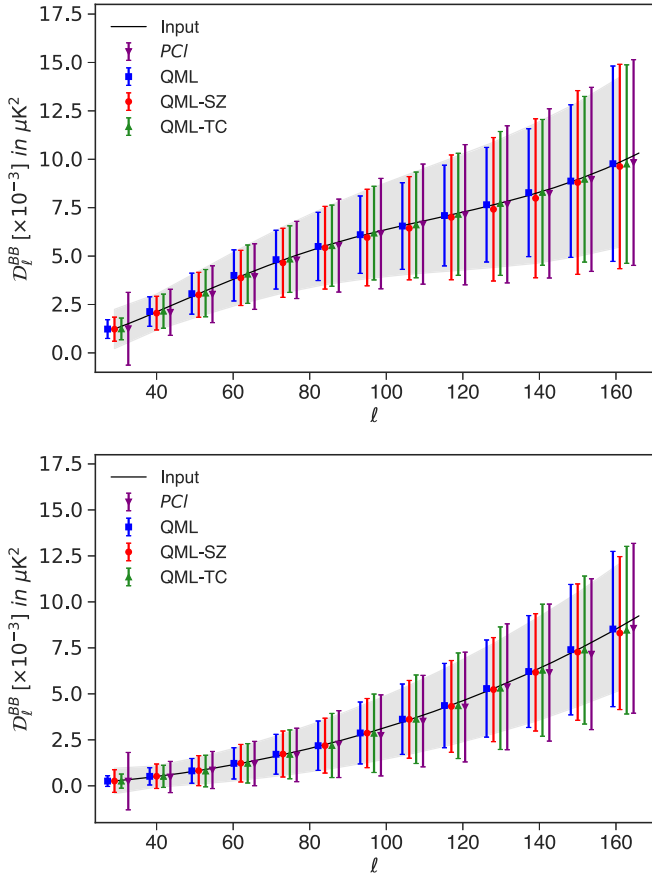
Figure 16. Plot of the results of B-mode power spectrum estimates for a realistic ground-based CMB experiment with inhomogeneous noise for $r = 0.05$ (upper panel) and $r = 0$ (lower panel), respectively. The observed sky with inhomogeneous noise is simulated at NSIDE = 512 with $\ell_{max} = 1024$. The input B-mode power spectrum is shown with the black solid curve. The classic QML method results are computed at NSIDE = 64 with $\ell_{max} = 192$ (blue square markers), the QML-SZ method results are computed at NSIDE = 64 with $\ell_{max} = 192$ (red, circle markers), and the QML-TC method results are also computed at NSIDE = 64 with $\ell_{max} = 192$ (green triangle markers). We also show the PCL estimator results, obtained with NaMaster using $\delta_c = 10°$ for both $r = 0.05$ and $r = 0$ (purple inverted triangle markers). The gray region denotes the analytical error bounds. The data points are means of 1000 estimates and the error bars are given by the standard deviation of the samples.

intend to compare the results of these QML methods with the PCL estimators. For PCL estimators, we smooth the masked *TQU* map with a Gaussian smoothing with FWHM = 20′ and directly analyze these maps without the downgrading process.

4.1. Space-based Experiment: Homogeneous Noise

The space-based experiments have a major advantage of being able to observe the full sky. However, the Galactic plane must be masked out due to the strong polarized foreground contribution from our Galaxy. Even though part of the sky must be removed to avoid the astrophysical Galactic contamination, satellite experiments are our best bet for observing the largest angular modes. For the satellite case, we set our target to NSIDE = 16 and $\ell_{max} = 32$ for all three QML estimators. The *QU* and scalar maps at NSIDE = 512 are downgraded to the targeted NSIDE = 16, using the ud_grade Healpix subroutine, as well as the masks, setting any pixel with values <0.99 to zero. Note that in this section, for the QML-SZ estimator, we downgrade the apodized mask instead of the binary mask, as

the SZ method uses an apodized mask. We multiply this downgraded mask to the downgraded maps. These are our input maps for QML estimators. We will compare these results with the PCL estimator results.

The results for this first case are shown in Figure 8 for both $r = 0.05$ and $r = 0$. We plot the mean of the power spectra estimates from 1000 simulations with error bars given by the standard deviation of these samples. In addition, we plot the results of the pure B-mode PCL estimator for the same case. The PCL results are obtained with C2 apodization with δ_c of 6°. We find that all of the QML methods outperform the PCL results in the entire multipole range. We notice that while the standard QML method has near optimal error bars throughout the entire multipole range, the QML-SZ method has suboptimal error bars for the lowest multipoles because we downgrade the input map, as discussed in Section 3.2.

That said, all QML estimators are tested with the same binary mask as defined in Section 3.2. However, for the QML-SZ estimator, we use the Gaussian apodized window to replace the binary mask, which causes the effective f_{sky} of the QML-SZ estimator to be smaller than that for the standard QML one and enlarges the uncertainties of the QML-SZ estimator for the entire multipole range. While the performance of the QML-SZ estimator is not as good as that of the standard QML method, it is still a fast and reliable solution for power spectrum estimation, except for the lowest few multipoles.

Due to the partial sky analysis, the coupling between different multipoles is inevitable. In order to quantify it, we calculate the normalized covariance matrices defined as

$$\mathcal{C}_{\ell\ell'} = \frac{\mathrm{cov}(\hat{C}_\ell^{BB}, \hat{C}_{\ell'}^{BB})}{\sqrt{\mathrm{var}(\hat{C}_\ell^{BB})\mathrm{var}(\hat{C}_{\ell'}^{BB})}}, \qquad (51)$$

and present the results in Figure 9. For the space-based experiment considering homogeneous noise, the power spectra estimates only weakly couple among different multipoles for every QML method tested here, with the covariance matrices being approximately diagonal.

4.2. Space-based Experiment: Inhomogeneous Noise

In this subsection, we will study the performance of the QML methods for a satellite experiment with inhomogeneous noise. We generate inhomogeneous noise maps using the hitmap for Planck HFI 100 GHz channel (shown in Figure 10) following the prescription given in Ducout et al. (2013). We set the white noise level of these maps ($\sigma_{\mathrm{isotropic\ noise}}$ of Ducout et al. 2013) to 5 μK arcmin. All of the calculation steps and parameters are consistent with the last subsection. We will still compare the results for the QML methodology with the ones for the PCL estimator.

The results for this case are shown in Figure 11, where the upper and lower panels represent $r = 0.05$ and $r = 0$, respectively. Comparing the results for the different methods with inhomogeneous noise, we can find that the different QMLs still outperform the PCL in our entire multipole range. The standard QML method still have near optimal error bars throughout the entire multipole range, while the QML-SZ method has slightly larger error bars for the lowest multipoles.

We also show the normalized covariance matrices for the power spectra estimators with the QML methods for this case in Figure 12. Similarly, we find that the covariance matrices are
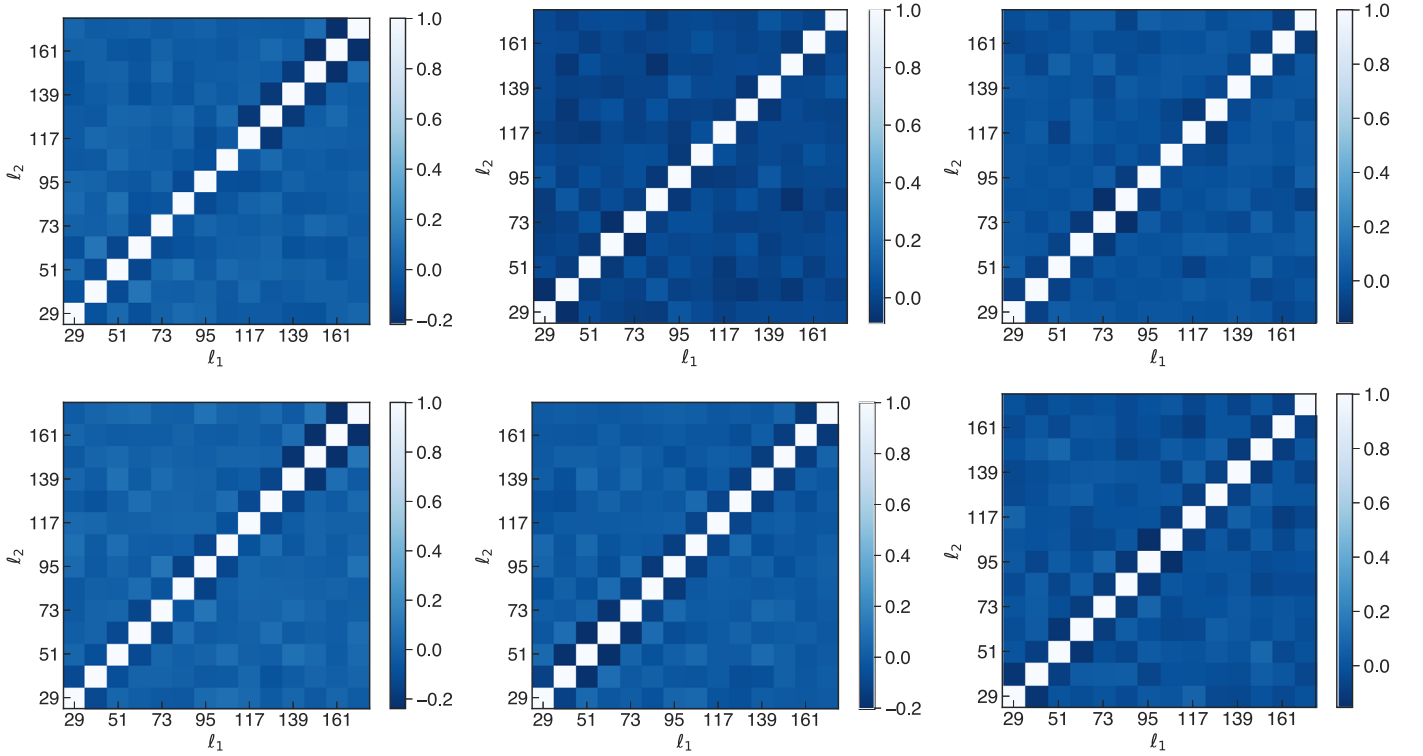
Figure 17. Same as Figure 14, but here we consider the inhomogeneous noise case for a ground-based experiment.

approximately diagonal, which indicates that the cross-correlations between different modes are weak for the presented QML methods.

4.3. Ground-based Experiment: Homogeneous Noise

Ground-based CMB experiments cannot account for full sky observations, since they are limited by their geographical location in terms of the total sky area available for the survey. That said, they have longer mission plans, during which they undergo instrumental upgrades that allow for higher sensitivity. For a ground-based survey, f_{sky} is usually quite small. For most cases, we have $f_{sky} \lesssim 10\%$, which allows us to choose larger NSIDE, in comparison with the ones chosen for the space-based experiment case.

For the analysis in this subsection, we downgrade the high resolution maps to NSIDE $= 64$ ($\ell_{max} = 192$) for all three QML methods. As in our previous examples, we also compare these QML results with the pure B-mode PCL estimator, obtained with C2 apodization. The apodization length δ_c is set to $6°$ and $10°$ for $r = 0.05$ and $r = 0$, respectively.

The process we use for suppressing the higher multipoles in the simulated maps at high resolution is the major difference between a ground-based and space-based experiment. Instead of smoothing the map, we start by obtaining the spherical harmonic coefficients of the maps at NSIDE $= 512$. We set all harmonic coefficients to zero above ℓ_{max} values stated above. We use the $a_{\ell m}$ values with this cutoff to reconstruct the map at NSIDE $= 512$, but remove the information above ℓ_{max}. This methodology is applied to the QU maps at NSIDE $= 512$ with $\ell_{max} = 192$, and to the scalar $\mathcal{B}$ and B-mode maps at

NSIDE $= 512$ with $\ell_{max} = 192$, too. Then we downgrade the map to the targeted NSIDE of 64.

In this subsection, we consider the homogeneous noise with the 3 μK arcmin noise level to study the performance of the QML methods on a small sky patch. The results for the power spectrum estimator are shown in Figure 13, from which we find that all of the methods discussed here give unbiased estimates of the B-mode band powers for both the $r = 0$ and $r = 0.05$ cases. However, when we focus on the error bars, the $r = 0$ and $r = 0.05$ cases have obvious differences. For $r = 0.05$, all of the methods (QMLs and PCL) have near optimal error bars in the entire multipole range.

However, for the $r = 0$ case, the CMB signal of the B-mode for $\ell < 60$ is so weak that the error bars are too small, and we cannot tell which method performs better. However, for $\ell > 60$, we find that all QML methods have smaller error bars than those for the PCL method. This means that, for the case with small r, QML methods perform better in reconstructing the B-mode power spectrum. In Figure 14, we have shown the normalized covariance matrices for the power spectra estimates with the three QML methods for this case. For the ground-based experiment, we also find our covariance matrices to be approximately diagonal, showing that the band power leakages have been suitably removed.

4.4. Ground-based Experiment: Inhomogeneous Noise

In this subsection, we will study the performance of the QML methods with the noise profile of the AliCPT-1 experiment as a realistic example. A map of the noise standard deviation per pixel for AliCPT-1 is shown in Figure 15. The major difference between the inhomogeneous noise case and

Table 1
Performance Comparison for Different Estimators in the Space-based Example

Estimator	NSIDE	N_d	ℓ_{max}	RAM (GB)	Time (s)
QML	16	4454	47	29.2	∼510
QML-SZ	16	2131	47	3.6	∼34

Table 2
Performance Comparison for Different Estimators in the Ground-based Example

Estimator	NSIDE	N_d	ℓ_{max}	RAM (GB)	Time (s)
QML	64	13,856	192	157.6	∼15,278
QML-SZ	64	6297	192	18.8	∼341
QML-TC	64	6859	192	21.8	∼431

homogeneous noise case is the way we deal with the noise. QML methods require a precise knowledge of the pixel noise matrix N to compute the bias term b_l in Equation (11). For the homogeneous case, the noise covariance matrix is a diagonal matrix with all diagonal elements equal, and we can calculate N with the noise power spectrum directly. However, in the inhomogeneous case, it is difficult to characterize the noise covariance matrix by an analytical formula. Here, we estimate the noise covariance matrix from numerical simulations. We generate 1000 noise samples and use the SZ method (or the TC method) to produce scalar noise maps of the QML-SZ method (or the QML-TC method). Then, we downgrade the scalar noise maps, as well as the original noise maps, to the targeted resolution. The covariance matrices of these noise-only simulations are the N matrices that we use in this case.

The corresponding results are shown in Figure 16. We find that all of the QML-based methods, as well as the PCL method, give unbiased estimates for the B-mode band powers for both $r = 0$ and $r = 0.05$. Let us focus on the $r = 0.05$ situation first. Comparing the QML results with that of the PCL method, we find that all of the QML methods have near optimal error bars in the entire multipole range, while for the PCL method, uncertainties increase rapidly with increasing angular scale. The QML methods have significant advantages on large scales for $r = 0.05$. For $r = 0$, the QML methods still keep their excellent performance on large scales, and in addition, we find that, even for the small scale, the QML methods outperforms the PCL method.

In Figure 17, we also show the normalized covariance matrices for the power spectra estimates for the three QML methods for this case. Similarly, we find that the covariance matrices are nearly diagonal, which indicates that the correlations between different bands are negligible.

4.5. Computational Performance

In Section 3, we discussed that the computational complexity of the QML estimator is a $O(N_d^3)$ problem, where N_d is the length of the data vector. We also discussed that N_d for the QML-SZ method or the QML-TC method is half of the N_d for the polarization part of the "reshaped" classical QML estimator for polarization. This reduces the computational requirements for the new QML methods. In Tables 1 and 2, we summarize the computational parameters for the three QML estimators for the space-based and ground-based experiment cases, respectively. We run all our computations on an Intel Xeon E2620 2.10 GHz workstation and list NSIDE, N_d, ℓ_{max}, RAM (in gigabytes), and computation time for a single computation.

As shown in Table 1, for the QML-SZ estimators, the computation time is only about 1/13 of that for the classic QML estimator. This happens because the data vector size, N_d, for the scalar QML method is about half of that for the classic QML method. Additionally, as both the QML-SZ and QML-TC methods are based on the scalar-mode QML method, its algorithm complexity is less than for the polarization mode,

and thereby the computation is faster. In Table 2, we show the same set of parameters for the ground-based experiment case. In this example, we compute all three QML methods at NSIDE = 64. And as shown in Table 2, the two scalar QML methods save on both computation time and memory requirements. Comparing with the results listed in the Table 1, we find that as N_d is increased, the advantages of the two scalar QML methods in terms of computation time become more obvious. In the scalar QML methods there is no need to calculate the rotation angle and perform coordinate transformation of Equation (13), and the signal covariance matrix is easier to compute with less memory overhead. For the ground-based case, the two scalar QML methods are near optimal in the multipole range of interest in this case, and their computational requirements mean that they can be applied on higher resolution maps to compute the power spectrum at higher multipoles.

5. Discussions and Conclusions

In this work, we introduce two novel QML estimators for the CMB B-mode power spectrum. Both of them are motivated by methods that isolate the CMB B-mode polarization information from the E-modes and "ambiguous" modes. Our method relies on the ability to construct a scalar map with only the B-mode information, which allows us to use a scalar QML estimator to obtain the CMB B-mode power spectrum. This reduces the computational requirements (both the memory requirement and computation time) in comparison to those for the traditional QML estimator for CMB polarization. From the space-based experiment example, we find that, at the same resolution, the new scalar QML methods give us more than 10 times improvement in computation time and more than 8 times reduction in the memory requirement.

The benefit of the computation efficiency is that the new scalar QML methods are a realistic solution for estimating the B-mode power from higher resolution maps, which allows us to extend the use of this method to higher multipoles. We have shown the application of them in the ground-based example, where the low computational requirements of the new QML methods allow us to make computations at a higher resolution, so we can get band power estimates to a larger multipole range.

In our tests, we find that both estimators give unbiased CMB power spectrum estimates for all cases we considered here. For the space-based mission case with large sky surveys, we find that the QML-SZ method is suboptimal for $\ell \leqslant 5$, while it performs nearly optimally for the rest of the multipole range. From the downgrading tests, we find that this increase in the error bars is likely linked to the effects of ud_grade on the $\mathcal{B}$-mode map. These errors might be reduced further by making a further optimization to the downgrading method, which we will postpone to a future work.

For the ground-based experiment (a small sky patch), the performance of both scalar QML methods is near optimal in the multipole range of interest. With low computational requirements, we can apply the new methods at higher resolution and obtain the band powers at high multipoles with minimum variance. The performance comparison for the ground-based case shows that both the QML-SZ and QML-TC methods make substantial improvements in terms of computational requirements over the traditional QML with some increase in the error bars. In addition, when comparing with the PCL method, we find that for $r = 0$, QML methods have smaller errors in the entire multipole range of analysis for both homogeneous and inhomogeneous noise. For $r = 0.05$, the QML methods have an obvious advantage at large scales in the inhomogeneous noise case.

In this work, we also perform idealized tests that consider the effects of the mask and downgrading the input maps and the impact of the noise level for the QML methods. From these tests, we conclude that the scalar QML methods are suitably adapted to applications that consider complex sky masks, and/ or different noise levels. We also find that the downgrading process would require further optimization to improve the performance of the QML-SZ method at low multipoles. We should mention that, in this paper, we have not considered other complications in the CMB observations, like correlated noise, foreground residuals, timestream filtering effects, and so on, which would certainly need to be tested for applicability in real data. We postpone these tests and optimizations of our novel methods to a future work.

In conclusion, we can summarize this work as a combination of constructing the pure B-mode polarization maps and constructing the scalar QML estimator. Recent proposals of isolating the B-mode information without ambiguous modes allow us to reduce the computational requirements of the problem without sacrificing on the size of error bars. Thus, we can extend the use of a minimum variance power spectrum estimator for B modes to higher resolution maps. These novel QML estimators for the B-mode power spectrum will hopefully be useful for future CMB B-mode experiments.

Appendix A
Miscellaneous Mathematical Relations

For an arbitrary function $_s f(\hat{n})$ with spin s, we can define (Newman & Penrose [1966]):

$$\eth_s f(\hat{n}) \equiv -\sin^s \theta \left(\frac{\partial}{\partial \theta} + \frac{i}{\sin \theta} \frac{\partial}{\partial \phi} \right) \sin^{-s} \theta \, _s f(\hat{n}), \quad (A1)$$

$$\bar{\eth}_s f(\hat{n}) \equiv -\sin^{-s} \theta \left(\frac{\partial}{\partial \theta} - \frac{i}{\sin \theta} \frac{\partial}{\partial \phi} \right) \sin^s \theta \, _s f(\hat{n}). \quad (A2)$$

Thus, the spin-weighted spherical harmonics are obtained by applying the spin-raising and spin-lowering operators ($\eth$ and $\bar{\eth}$) on the standard (spin-0) spherical harmonics:

$$_s Y_{\ell m} = \frac{1}{N_{l,s}} \eth^s Y_{\ell m}, \qquad _{-s} Y_{\ell m} = \frac{(-1)^s}{N_{l,s}} \bar{\eth}^s Y_{\ell m}. \quad (A3)$$

They have the property: $_s Y_{\ell m}^* = (-1)^{s+m} \, _{-s} Y_{\ell(-m)}$. The functions F_ℓ^{10}, F_ℓ^{12}, and F_ℓ^{22} below Equation (15) are given by

$$F_\ell^{10}(z) = 2 \frac{\frac{\ell z}{1-z^2} P_{\ell-1}(z) - \left(\frac{\ell}{1-z^2} + \frac{\ell(\ell-1)}{2} \right) P_\ell(z)}{[(\ell-1)\ell(\ell+1)(\ell+2)]^{1/2}}$$

$$F_\ell^{12}(z) = 2 \frac{\frac{(\ell+2)z}{1-z^2} P_{\ell-1}^2(z) - \left(\frac{\ell-4}{1-z^2} + \frac{\ell(\ell-1)}{2} \right) P_\ell^2(z)}{(\ell-1)\ell(\ell+1)(\ell+2)}$$

$$F_\ell^{22}(z) = 4 \frac{(\ell+2) P_{\ell-1}^2(z) - (\ell-1) z P_\ell^2(z)}{(\ell-1)\ell(\ell+1)(\ell+2)(1-z^2)},$$

where the P_ℓ and P_ℓ^2 denote associated Legendre polynomials P_ℓ^m for the cases $m = 0$ and $m = 2$. We can use the property of spin-raising and -lowering operators on Equations (31) and (32), such that they assume the form (Ferté et al. [2013]):

$$\tilde{\mathcal{E}}_{\ell m} = -\frac{1}{2} \int d\hat{n} [P_+((\bar{\eth}\bar{\eth}W) Y_{\ell m}^* + 2 N_{\ell,1}(\bar{\eth}W) _1 Y_{\ell m}^* + N_{\ell,2} W _2 Y_{\ell m}^* $$
$$+ P_-((\eth\eth W) Y_{\ell m}^* - 2 N_{\ell,1}(\eth W) _{-1} Y_{\ell m}^* + N_{\ell,2} W _{-2} Y_{\ell m}^*)], \quad (A4)$$

$$\tilde{\mathcal{B}}_{\ell m} = -\frac{1}{2i} \int d\hat{n} [P_+((\bar{\eth}\bar{\eth}W) Y_{\ell m}^* + 2 N_{\ell,1}(\bar{\eth}W) $$
$$\times \, _1 Y_{\ell m}^* + N_{\ell,2} W _2 Y_{\ell m}^*) $$
$$- P_-((\eth\eth W) Y_{\ell m}^* - 2 N_{\ell,1}(\eth W) _{-1} Y_{\ell m}^* + N_{\ell,2} W _{-2} Y_{\ell m}^*)], \quad (A5)$$

where

$$\bar{\eth}W = -\frac{\partial W}{\partial \theta} - \frac{i}{\sin \theta} \frac{\partial W}{\partial \phi},$$

$$\bar{\eth}\bar{\eth}W = -\cot \theta \frac{\partial W}{\partial \theta} + \frac{\partial^2 W}{\partial \theta^2} - \frac{1}{\sin \theta^2} \frac{\partial^2 W}{\partial \phi^2}$$

$$- \frac{2i \cot \theta}{\sin \theta} \frac{\partial W}{\partial \phi} + \frac{2i}{\sin \theta} \frac{\partial^2 W}{\partial \theta \partial \phi}.$$

Appendix B
Template Cleaning Residuals

We have stated in Section 4 that for satellite experiment cases we do not use the QML-TC method due to the presence of residuals after cleaning the maps by the template cleaning method. After cleaning with the leakage template, the cleaned B-mode maps have residuals that cannot be ignored for an unbiased recovery of the power at the largest scales. In Figure 18 we show the residuals for template cleaned B maps with the Planck mask and without noise. From Figure 18, we can see that most residuals are largely limited to the boundary of the observed patch. These may be removed by additionally masking $3°$ inside from the boundary of the mask. On removing the edge we can see most of the residual is removed,
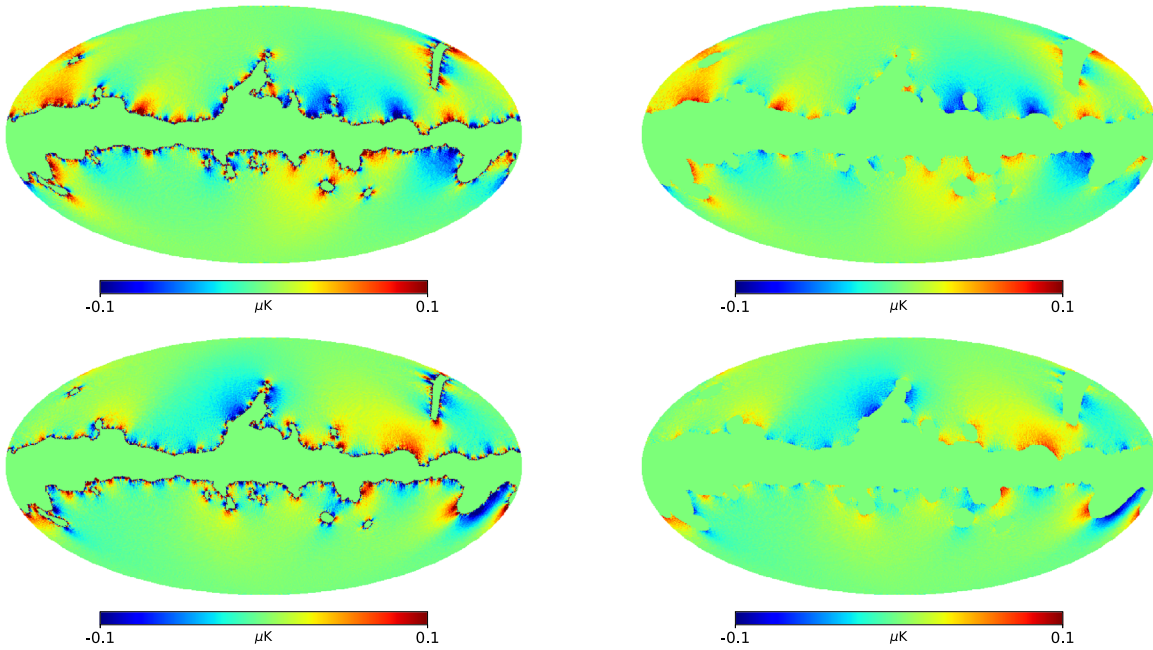
Figure 18. Residual *B* maps after template cleaning. The left panel shows the results with the Planck mask and the right panel shows the results with 3° removed from the edge. The upper panel shows the results for an input cosmological model with $r = 0.05$, while the lower panel shows the results for $r = 0$.

leaving behind residual contaminations on the large angular scales. The presence of these residuals means that the QML-TC method does not give unbiased power spectrum estimates. In the $r = 0.05$ case the power spectra estimates are biased for $\ell < 4$ and unbiased everywhere else. When $r = 0$, we found it more challenging to obtain unbiased power spectrum estimates for the low multipoles. We have tried various lengths of cuts from the edge of the mask; however, our results did not improve significantly. Thus the large angular scale *B*-mode residuals from template cleaning make it difficult to obtain unbiased power spectrum estimates at low multipoles. For this reason the QML-TC method is unsuitable for use in the satellite experiment cases, where we hope to recover the power on the largest angular scale correctly.

We conclude that the QML-TC method needs further optimization for application in satellite experiments. It may be possible to modify the template cleaning procedure to reduce or remove the residuals, or we can even look to account for the residual in the QML-TC pipeline. However, we will postpone any such modifications to a future work.

ORCID iDs

Jiming Chen ⬤ https://orcid.org/0000-0002-7679-0614
Shamik Ghosh ⬤ https://orcid.org/0000-0002-7546-0509
Hao Liu ⬤ https://orcid.org/0000-0002-1802-6917
Le Zhang ⬤ https://orcid.org/0000-0002-1182-8888
Bin Hu ⬤ https://orcid.org/0000-0001-5093-8118
Wen Zhao ⬤ https://orcid.org/0000-0002-1330-2329

References

Ade, P., Aguirre, J., Ahmed, Z., et al. 2019, JCAP, 2019, 056
Ahmed, Z., Amiri, M., Benton, S. J., et al. 2014, Proc. SPIE, 9153, 91531N
Alonso, D., Sanchez, J., Slosar, A. & LSST Dark Energy Science Collaboration 2019, MNRAS, 484, 4127
Baskaran, D., Grishchuk, L. P., & Polnarev, A. G. 2006, PhRvD, 74, 083008
Benabed, K., Bernardeau, F., & van Waerbeke, L. 2001, PhRvD, 63, 043501
Benson, B. A., Ade, P. A. R., Ahmed, Z., et al. 2014, Proc. SPIE, 9153, 91531P
BICEP2/Keck CollaborationPlanck Collaboration, Ade, P. A. R., et al. 2015, PhRvL, 114, 101301
Brown, M. L., Ade, P., Bock, J., et al. 2009, ApJ, 705, 978
Bucher, M., Moodley, K., & Turok, N. 2001, PhRvL, 87, 191301
Bunn, E. F. 2008, arXiv:0811.0111
Bunn, E. F. 2011, PhRvD, 83, 083003
Bunn, E. F., & Wandelt, B. 2017, PhRvD, 96, 043523
Bunn, E. F., Zaldarriaga, M., Tegmark, M., & de Oliveira-Costa, A. 2003, PhRvD, 67, 023501
Cao, L., & Fang, L.-Z. 2009, ApJ, 706, 1545
Chiang, H. C., Ade, P. A. R., Barkats, D., et al. 2010, ApJ, 711, 1123
Ducout, A., Bouchet, F. R., Colombi, S., Pogosyan, D., & Prunet, S. 2013, MNRAS, 429, 2104
Efstathiou, G. 2004, MNRAS, 349, 603
Efstathiou, G. 2006, MNRAS, 370, 343
Ferté, A., Grain, J., Tristram, M., & Stompor, R. 2013, PhRvD, 88, 023524
Flauger, R., & Weinberg, S. 2007, PhRvD, 75, 123505
Ghosh, S., Delabrouille, J., Zhao, W., & Santos, L. 2021, JCAP, 2021, 036
Giovi, F., Baccigalupi, C., & Perrotta, F. 2003, PhRvD, 68, 123002
Górski, K. M., Hivon, E., Banday, A. J., et al. 2005, ApJ, 622, 759
Grain, J., Tristram, M., & Stompor, R. 2009, PhRvD, 79, 123515
Grain, J., Tristram, M., & Stompor, R. 2012, PhRvD, 86, 076005
Grishchuk, L. P. 1974, ZhETF, 67, 825
Hansen, F. K., & Górski, K. M. 2003, MNRAS, 343, 559
Hazumi, M., Ade, P. A. R., Akiba, Y., et al. 2019, JLTP, 194, 443
Henderson, S. W., Allison, R., Austermann, J., et al. 2016, JLTP, 184, 772
Henning, J. W., Sayre, J. T., Reichardt, C. L., et al. 2018, ApJ, 852, 97
Hinshaw, G., Nolta, M. R., Bennett, C. L., et al. 2007, ApJS, 170, 288
Hivon, E., Górski, K. M., Netterfield, C. B., et al. 2002, ApJ, 567, 2
Hu, W., Spergel, D. N., & White, M. 1997, PhRvD, 55, 3288
Jewell, J., Levin, S., & Anderson, C. H. 2004, ApJ, 609, 1
Kamionkowski, M., Kosowsky, A., & Stebbins, A. 1997, PhRvL, 78, 2058
Kim, J. 2011, A&A, 531, A32
Kim, J., & Naselsky, P. 2010, A&A, 519, A104
Kodi Ramanah, D., Lavaux, G., & Wandelt, B. D. 2018, MNRAS, 476, 2825
Kodi Ramanah, D., Lavaux, G., & Wandelt, B. D. 2019, MNRAS, 490, 947
Komatsu, E., Smith, K. M., Dunkley, J., et al. 2011, ApJS, 192, 18
Kovac, J. M., Leitch, E., Pryke, C., et al. 2002, Natur, 420, 772
Larson, D. L., Eriksen, H. K., Wandelt, B. D., et al. 2007, ApJ, 656, 653
Lewis, A. 2003, PhRvD, 68, 083509
Lewis, A., Challinor, A., & Lasenby, A. 2000, ApJ, 538, 473

Li, H., Li, S.-Y., Liu, Y., et al. 2017, arXiv:1710.03047
Liddle, A. R., & Lyth, D. H. 2000, Cosmological Inflation and Large-scale Structure (Cambridge: Cambridge Univ. Press)
Linde, A., Sasaki, M., & Tanaka, T. 1999, PhRvD, 59, 123522
Liu, H., Creswell, J., & Dachlythra, K. 2019b, JCAP, 2019, 046
Liu, H., Creswell, J., von Hausegger, S., & Naselsky, P. 2019a, PhRvD, 100, 023538
Louis, T., Næss, S., Das, S., Dunkley, J., & Sherwin, B. 2013, MNRAS, 435, 2040
Ma, Y.-Z., Zhao, W., & Brown, M. L. 2010, JCAP, 2010, 007
Montroy, T. E., Ade, P. A. R., Bock, J. J., et al. 2006, ApJ, 647, 813
Naess, S., Hasselfield, M., McMahon, J., et al. 2014, JCAP, 2014, 007
Newman, E. T., & Penrose, R. 1966, JMP, 7, 863
Pérez-de-Taoro, M. R., Aguiar-González, M., Génova-Santos, R., et al. 2014, Proc. SPIE, 9145, 91454T
Planck Collaboration, Ade, P. A. R., Aghanim, N., et al. 2014, A&A, 571, A16
Planck Collaboration, Aghanim, N., Akrami, Y., et al. 2020, A&A, 641, A6
Pritchard, J. R., & Kamionkowski, M. 2005, AnPhy, 318, 2
QUIET Collaboration, Araujo, D., Bischoff, C., et al. 2012, ApJ, 760, 145
Salatino, M., Austermann, J. E., Thompson, K. L., et al. 2021, arXiv:2101.09608
Santos, L., Wang, K., Hu, Y., Fang, W., & Zhao, W. 2017, JCAP, 2017, 043

Santos, L., Wang, K., & Zhao, W. 2016, JCAP, 2016, 029
Seljak, U., & Zaldarriaga, M. 1996, ApJ, 469, 437
Seljak, U., & Zaldarriaga, M. 1997, PhRvL, 78, 2054
Smith, K. M. 2006, PhRvD, 74, 083002
Smith, K. M., & Zaldarriaga, M. 2007, PhRvD, 76, 043001
Tegmark, M. 1997, PhRvD, 55, 5895
Tegmark, M., & de Oliveira-Costa, A. 2001, PhRvD, 64, 063001
The CMB-S4 Collaboration, Abazajian, K., et al. 2020, arXiv:2008.12619
The LSPE Collaboration, Aiola, S., Amico, G., et al. 2012, arXiv:1208.0281
Vanneste, S., Henrot-Versillé, S., Louis, T., & Tristram, M. 2018, PhRvD, 98, 103526
Wandelt, B. D., Larson, D. L., & Lakshminarayanan, A. 2004, PhRvD, 70, 083511
Wang, Y.-F., Wang, K., & Zhao, W. 2016, RAA, 16, 59
Zaldarriaga, M., & Seljak, U. 1997, PhRvD, 55, 1830
Zaldarriaga, M., & Seljak, U. 1998, PhRvD, 58, 023003
Zhao, W., & Baskaran, D. 2010, PhRvD, 82, 023001
Zhao, W., Baskaran, D., & Grishchuk, L. P. 2009, PhRvD, 79, 023002
Zhao, W., Baskaran, D., & Grishchuk, L. P. 2010, PhRvD, 82, 043003
Zhao, W., & Grishchuk, L. P. 2010, PhRvD, 82, 123008
Zhao, W., & Zhang, Y. 2006, PhRvD, 74, 083006